PERGAMON

International Journal of Multiphase Flow 27 (2001) 1965–2000

International Journal of Multiphase Flow

www.elsevier.com/locate/ijmulflow

A two-equation turbulence model of turbulent bubbly flows

A.A. Troshko, Y.A. Hassan *

Department of Nuclear Engineering, Texas A&M University, College Station, TX 77843-3133, USA

Received 30 August 2000; received in revised form 21 June 2001

Abstract

A two-fluid model of turbulent, adiabatic bubbly flow was implemented in the computational fluid dynamics (CFD) CFX4.2 program and validated. Turbulence in the dispersed (bubble) phase was neglected. Liquid turbulence was modeled through a two-phase extension of the single-phase standard k–ε model. Conservation equations of turbulent scales contain single-phase and interfacial terms. A closure for the interfacial turbulence terms was proposed based on the assumption of low-bubble inertia and neglecting surface tension. The interfacial turbulence terms account for additional pseudoturbulence in liquid created by bubble-induced mixing. The proposed turbulence model contained the single empirical constant in the modeled dissipation rate balance. The model was implemented in the CFX4.2 commercial CFD solver. Comparing numerical predictions to the experimental data the value of the model constant was estimated. Model predictions were compared to other bubbly flows to prove the universality of the model constant. The comparison showed that the constant has a certain generality. A new, two-phase logarithmic wall law was also implemented and validated. The derivation of the new law was based on an assumption of the additional eddy diffusivity due to the bubble-induced stirring in the boundary layer. An improved wall friction prediction was achieved with the new wall law over conventional single-phase law. The improvement was especially noticeable for the low-liquid flow rates when bubble-induced pseudoturbulence plays a significant role. The ability of the model to account for bubble size effect was also studied.

1. Introduction

Bubbly flows consist of gas bubbles (dispersed phase) within a carrier liquid (continuous phase). Examples of industrial bubbly flows include all types of boiling heat transfer, bubble stirred chemical reactors etc. Knowledge of the characteristics of bubbly flows is important in the

* Corresponding author. Tel.: +1-979-845-7090; fax: +1-979-845-6443.
E-mail address: y-hassan@tamu.edu (Y.A. Hassan).

0301-9322/01/$ - see front matter
PII: S0301-9322(01)00043-X

design of multi-fluid systems. As the computer power dramatically increases each year, it is desirable to employ advanced multi-dimensional models to calculate bubbly flows more precisely through methods of computational fluid dynamics (CFD). These models should be able to account for such effects as turbulence, strong interaction between phases and multi-dimensionality, which are the general attributes of the most of bubbly flows. The models should also rely on the empirical data to the least possible extent.

Several two-fluid CFD models of bubbly turbulent flows were reported in the literature. As an example, Lopez de Bertodano (1992) used two-phase extension of the algebraic stress model (ASM) to model turbulence effects in the liquid phase. The turbulence scale equations were derived on the presumption that the total liquid turbulence is a sum of shear and bubble-induced components. Total liquid eddy diffusivity was modified by an addition of the bubble-induced eddy diffusivity introduced by Sato et al. (1981). A comparison of this model's prediction with experimental data on bubbly flows, in a vertical duct, gave encouraging results. Morel (1997) used a two-phase extension of k–ε model to describe liquid turbulence. In his model, bubble-induced modification to liquid turbulence was accounted for by an additional production term in the liquid turbulent energy balance. This term was proportional to the work of the interfacial force per unit of time. In the dissipation rate balance, the rate of destruction of bubble-induced turbulence was modeled by multiplying the bubble production term by a characteristic frequency. This frequency was calculated from the turbulence dissipation rate and the bubble diameter, based on the dimensional analysis. All models described above relied on the single-phase wall function approach as a smooth wall boundary condition. This is, obviously, in a contradiction to the experimental results of Marié et al. (1997), Nakoryakov et al. (1981, 1996) and Sato et al. (1981). Their experiments have shown that liquid velocity obeys the logarithmic law. However, the wall law constants become functions of the flow parameters, if boundary layer bubble concentration was significant.

The present research is intended as a continuation of the previous efforts to create a practical model of turbulent bubbly flows. First, two-fluid model of adiabatic, incompressible bubbly flows is described with an emphasis on the all-important interfacial forces. Second, a new model for liquid turbulence is proposed. Third, a new logarithmic wall law for bubbly boundary layer proposed by Troshko and Hassan (2001) is used. Fourth, results of the model validation are discussed and conclusions are drawn.

2. Governing equations

Drew (1983) and Kataoka (1986) used concept of phase indicator function to derive the microscopic conservation equations governing adiabatic incompressible two-phase flows. The phase indicator function was defined as

$$\theta_k(\mathbf{x},t) = \begin{cases} 1 & \text{if}(\mathbf{x},t) \text{ is occupied by phase } k, \\ 0 & \text{otherwise}, \end{cases} \tag{1}$$

where $\mathbf{x}$ is the space vector, t is time. Subscript k refers to phase, where $k = \mathrm{C}$ for continuous phase (liquid) or $k = \mathrm{D}$ for dispersed phase (bubbles). The obtained equations contained single-

phase terms and interfacial terms identified by the presence of indicator function gradient $\nabla\theta_k$. This gradient is zero everywhere except at the interface where it has a singular value

$$\nabla\theta_k = \mathbf{n}_k\delta(\mathbf{x} - \mathbf{x}_\mathrm{i}, t). \tag{2}$$

In Eq. (2), $\mathbf{n}_k$ is the unity vector normal to the interface and pointing outward in respect to the phase k, δ is the delta (Dirac) function and subscript i refers to the interface. The microscopic equations become singular at the interface, which is a direct consequence of the zero interface thickness assumption introduced in (1). The governing equations were ensemble averaged to remove such singularity. A general microscopic transported property ϕ was decomposed into average and fluctuating part (Kataoka, 1986)

$$\phi(\mathbf{x}, t) \equiv \langle\phi_k\rangle + \phi'_k, \tag{3}$$

where the phasic ensemble average is defined as

$$\langle\phi_k\rangle = \langle\theta_k\phi\rangle/\alpha_k. \tag{4}$$

In Eq. (4), $\langle\cdot\rangle$ is the operator of ensemble average and $\langle\theta_k\rangle = \alpha_k$ is the void fraction. Assuming both phases adiabatic and the fluids to be incompressible and neglecting surface tension, the following equations were obtained:

Mass

$$\frac{\partial\alpha_k}{\partial t} + \nabla\cdot(\alpha_k\mathbf{U}_k) = 0. \tag{5}$$

Momentum

$$\frac{\partial(\rho_k\alpha_k\mathbf{U}_k)}{\partial t} + \nabla\cdot(\rho_k\alpha_k\mathbf{U}_k\mathbf{U}_k) = -\alpha_k\nabla P_k + \nabla\cdot\left(\alpha_k\left(\mathbf{T}_k + \mathbf{T}_k^{Re}\right)\right) + \mathbf{M}_k + (p_\mathrm{i} - P_k)\nabla\alpha_k + \rho_k\alpha_k\mathbf{g}, \tag{6}$$

where $\mathbf{U}_k$, P_k, $\mathbf{T}_k$, $\mathbf{g}$ are the mean (ensemble averaged) velocity, pressure, viscous stress and gravitational acceleration, respectively. Interfacial pressure is defined as $p_\mathrm{i} = \langle p\nabla\theta_k\rangle\cdot\nabla\alpha_k|\nabla\alpha_k|^{-2}$ (Drew, 1983). Eq. (6) contains unknown terms such as $\mathbf{M}_k$ (interfacial force density), $p_\mathrm{i} - P_k$ (interfacial pressure difference), $\mathbf{T}_k^{Re}$ (Reynolds turbulent stress). All the unknown terms in the above equation are a result of the inevitable loss of information about the microscopic flow structure after the averaging process. Closure of these terms remains a challenging problem. In the past, considerable efforts were dedicated to the closure of the first two interfacial terms. Although still far from being widely accepted, the model presented below is the most up to date model in the case of dispersed bubbly flow.

2.1. Interfacial force density

It was assumed that there is no mass transfer between phases and the surface tension force is not important. Therefore, by Newton's law, interface force densities acting on each phase differ in sign only

$$\mathbf{M}_\mathrm{C} = -\mathbf{M}_\mathrm{D}. \tag{7}$$

Traditionally, the interfacial force density is decomposed into several components:

$$\mathbf{M}_C = \mathbf{F}_C^{drag} + \mathbf{F}_C^{vm} + \mathbf{F}_C^{lift} + \mathbf{F}_C^{wall} + \mathbf{F}_C^{td}. \tag{8}$$

Each of these components is associated with particular physical mechanism of the interfacial momentum transfer. A brief description of each interfacial force component is presented below.

The origin of the drag force is due to the resistance experienced by a body moving in the liquid. Viscous stress creates skin drag and pressure distribution around the moving body creates form drag. The later mechanism is due to inertia and becomes significant as the particle Reynolds number

$$Re_b = \frac{d|\mathbf{U}_r|}{v_C} \tag{9}$$

becomes larger. In Eq. (9), $\mathbf{U}_r = \mathbf{U}_D - \mathbf{U}_C$ is the slip velocity, d is the bubble equivalent diameter and v_C is the liquid kinematic viscosity. The drag force density is written in the following form:

$$\mathbf{F}_C^{drag} = \frac{3}{4}\frac{C_d}{d}\alpha_D\rho_C|\mathbf{U}_r|\mathbf{U}_r, \tag{10}$$

where C_d is the drag coefficient taking into account the character of the flow around the bubble. Hydrodynamic interaction of the bubble with other particles also influences the drag coefficient. This phenomenon can be taken into account (Ishii and Zuber, 1979).

Virtual mass force arises when there exists a relative acceleration between two phases

$$\mathbf{F}_C^{vm} = \alpha_D C_{vm}\rho_C\left(\frac{D_C\mathbf{U}_D}{Dt} - \frac{D_D\mathbf{U}_C}{Dt}\right), \tag{11}$$

where D_k/Dt is the material time derivative of the phase k. For the potential flow around single sphere, constant C_{vm} is equal to 0.5. If the hydrodynamic interaction between bubbles is significant, then C_{vm} becomes a function of α_D (Drew, 1983).

Lift force arises from the interaction between bubble and the shear stress in liquid. The general expression for the lift force density is

$$\mathbf{F}_C^{lift} = \alpha_D\rho_C C_l\mathbf{U}_r \times \nabla \times \mathbf{U}_C. \tag{12}$$

The sign of this force depends on the orientation of slip velocity with respect to the gravity vector. For example, in upward pipe flows this force pushes bubbles towards the wall. When flow is downward, it pushes bubbles to the pipe center. The value of the lift coefficient C_l ranges from 0.01 for the laminar flow to 0.5 for the inviscid flow around the sphere. Wang et al. (1987) found that coefficient C_l, in general, depends on the flow parameters. Lopez de Bertodano (1992) recommended $C_l = 0.1$ for bubbly flows in vertical pipes. Recently, Moraga et al. (1999) correlated C_l as a function of bubble and local shear Reynolds numbers. Moraga et al. also showed that C_l may be negative for large bubbles in high-shear flows.

The origin of the wall force is due to the fact that liquid flow rate between bubble and the wall is lower than between the bubble and the outer flow. This results in a hydrodynamic pressure difference driving bubble away from the wall. This force density is approximated as

$$\mathbf{F}_C^{wall} = \frac{\alpha_D\rho_C|\mathbf{U}_r|^2}{d}\max\left(0, C_{w1} + C_{w2}\frac{d}{y_w}\right)\mathbf{n}_w, \tag{13}$$

where $\mathbf{n}_w$ is the outward unit vector perpendicular to the wall and y_w is the distance from the wall to the bubble. Constants C_{w1} and C_{w2} determine the magnitude and the effective action distance, which is equal to dC_{w2}/C_{w1}.

The turbulent dispersion force, derived by Lopez de Bertodano (1992), is based on the analogy with molecular movement. It approximates a turbulent diffusion of the bubbles by the liquid eddies. It is formulated as

$$\mathbf{F}_C^{td} = -C_{td}\rho_C k_C \nabla\alpha_C, \tag{14}$$

where k_C is the liquid turbulent kinetic energy per unit of mass. Lopez de Bertodano (1992) suggested the value of coefficient C_{td} to be of order 0.1. Although Lopez de Bertodano did not justify this choice, it seems that it was chosen based on the similarity with the eddy diffusivity constant $C_\mu = 0.09$ in the single-phase k–ε model.

2.2. Interfacial pressure difference

Lamb (1932) considered the potential flow around single sphere. His result for the interfacial pressure difference is

$$(p_i - P_C) = -C_p\rho_C|\mathbf{U}_r|^2\alpha_C, \tag{15}$$

where $C_p = 0.25$. Lance and Bataille (1991) found that $0.6 \leqslant C_p \leqslant 1.7$ for the oblate spheroid shaped bubbles moving along helical trajectories. Lopez de Bertodano (1992) recommended $C_p = 1.0$ for bubbly flows in pipes. Drew (1983) argued that under the assumption of incompressibility of both phases and without bubble expansion/contraction there exists a microscopic instantaneous pressure equilibrium, i.e., $C_p = 0$. Furthermore, Drew (1983) also pointed out, that expression (15) describes the form drag effects, which was already taken into account by the drag force coefficient in (10). Thus, $C_p = 0$ was used in our current model. Note, that the microscopic pressure equilibrium assumption together with the neglect of the surface tension leads to the single pressure field shared by both phases: $P_C = P_D$.

It must be pointed out, that closure coefficients C_d, C_{vm}, C_l, C_{w1}, C_{w2} and C_{td} are rather flow dependent. Even for simple bubbly flows, there is a lack of knowledge about their values except, perhaps, drag and virtual mass coefficients. The reason is that it is very difficult to conduct separate effect experiments to estimate the value of these coefficients with a good accuracy.

3. Model of turbulence

In the previous chapter, constitutive equations were written for the interfacial momentum terms for the case of incompressible, adiabatic bubbly flows. Despite considerable efforts, accurate modeling of the interfacial force density remains an open question even for simple dispersed bubbly flows. Even less is known about two-phase turbulent Reynolds stress $\mathbf{T}_k^{Re}$ in (6), which is defined as

$$\mathbf{T}_k^{Re} = -\frac{\rho_k}{\alpha_k}\left\langle \theta_k \mathbf{U}_k' \mathbf{U}_k' \right\rangle, \tag{16}$$

where fluctuation velocity vector $\mathbf{U}_k'$ is defined in (3).

Experimental evidence (Serizawa et al., 1975) suggests that

$$\frac{\left\|\mathbf{T}_{\mathrm{D}}^{Re}\right\|}{\left\|\mathbf{T}_{\mathrm{C}}^{Re}\right\|} = O\left(\frac{\rho_{\mathrm{D}}}{\rho_{\mathrm{C}}}\right), \tag{17}$$

where $\|\ \|$ is some suitably defined norm. Since for the most of bubbly flows, $\rho_{\mathrm{C}}/\rho_{\mathrm{D}}$ density ratio is high, the magnitude of the dispersed phase (bubbles) Reynolds stress is much smaller than that in the continuous phase (liquid), i.e.

$$\left\|\mathbf{T}_{\mathrm{D}}^{Re}\right\| \ll \left\|\mathbf{T}_{\mathrm{C}}^{Re}\right\|. \tag{18}$$

It is commonly assumed that the concept of eddy diffusivity can be extended to the two-phase flows

$$\mathbf{T}_k^{Re} = \rho_k\left(v_k^{\mathrm{t}}\left(\nabla\mathbf{U}_k + (\nabla\mathbf{U}_k)^{\mathrm{T}} - \frac{2}{3}\mathbf{I}(\nabla\cdot\mathbf{U}_k)\right) - \frac{2}{3}\mathbf{I}k_k\right), \tag{19}$$

where v_k^{t} is the eddy diffusivity and superscript T denotes transposition. However, Wang et al. (1987) experimentally found that for some downward pipe bubbly flows, liquid Reynolds stress is not parallel to the mean strain rate tensor. Nevertheless, as a first approximation, Eq. (19) can be utilized. Then, the problem of eddy diffusivity modeling would arise. Again, single-phase k–ε model can be used as a first approximation

$$v_k^{\mathrm{t}} = C_\mu\frac{k_k^2}{\varepsilon_k}, \tag{20}$$

where turbulent kinetic energy per unit of mass (or simply turbulent energy) is defined as

$$k_k = \frac{1}{2\alpha_k}\left\langle\theta_k\mathbf{U}_k'\cdot\mathbf{U}_k'\right\rangle. \tag{21}$$

Turbulence dissipation rate ε_k per unit of mass (or simply dissipation rate) is defined as

$$\varepsilon_k = \frac{\left\langle\theta_k\left(\nabla\mathbf{U}_k'\right):\mathbf{T}_k'\right\rangle}{\alpha_k\rho_k}, \tag{22}$$

where the fluctuating part of viscous stress $\mathbf{T}_k'$ is determined by (3). Assuming the carrier liquid and gas are Newtonian fluids, Eq. (22) becomes

$$\varepsilon_k = \frac{\nu_k}{\alpha_k}\left(\left\langle\theta_k\nabla\mathbf{U}_k' : \nabla\mathbf{U}_k'\right\rangle + \left\langle\theta_k\nabla\mathbf{U}_k' : \left(\nabla\mathbf{U}_k'\right)^{\mathrm{T}}\right\rangle\right). \tag{23}$$

Single-phase equations (19) and (20) take into account interfacial effects implicitly. These effects are contained within values of k_k and ε_k. Thus, the transport equations for these turbulent scales must have interfacial effects explicitly. Kataoka and Serizawa (1989), Kashiwa and Gore (1991) and Troshko (2000) derived the exact balance equation for k_k using the same approach as was used to derive Eqs. (5) and (6). Under assumptions stated above, the turbulence balance equation can be cast as

$$\frac{\partial(\rho_k\alpha_k k_k)}{\partial t}+\nabla\cdot(\rho_k\alpha_k\mathbf{U}_k k_k)=\alpha_k\mathbf{T}_k^{Re}:(\nabla\mathbf{U}_k)$$
$$-\nabla\cdot\left(\frac{\rho_k\langle\theta_k\mathbf{U}_k'\left|\mathbf{U}_k'\right|^2\rangle}{2}+\langle\theta_k\mathbf{U}_k'P_k'\rangle-\langle\theta_k\mathbf{U}'\cdot_k\mathbf{T}_k'\rangle\right)$$
$$-\rho_k\alpha_k\varepsilon_k+\langle\mathbf{U}_{ki}'\cdot(\mathbf{T}_{ki}'-\mathbf{I}P_i')\cdot(\nabla\theta_k)\rangle. \tag{24}$$

In Eq. (24), the first term on the right-hand side is the single-phase production of turbulence by the mean strain rate. The second term is the diffusion by velocity fluctuations, pressure fluctuations and molecular viscosity, respectively. Third term is the dissipation. The last term describes interfacial transfer of turbulence. Since the gradient of the phase indicator function is non-zero at the interface, all fluctuation components in the interfacial term are defined as

$$\phi_{ki}'=\phi_{\mathrm{i}}(\mathbf{x},t)-\langle\phi_k\rangle. \tag{25}$$

Interfacial term in (24) can be identically rewritten as (Kataoka and Serizawa, 1989; Troshko, 2000):

$$\left\langle\mathbf{U}_{ki}'\cdot(\mathbf{T}_{ki}-\mathbf{I}P_{ki}')\cdot(\nabla\theta_k)\right\rangle=\langle((p-p_{\mathrm{i}})\mathbf{I}-\mathbf{t})\cdot\nabla\theta_k\cdot\mathbf{U}_k'\rangle+((p_{\mathrm{i}}-P_k)\mathbf{I}+\mathbf{T}_k):\langle\mathbf{U}_k'\nabla\theta_k\rangle, \tag{26}$$

where p and $\mathbf{t}$ are the microscopic pressure and viscous stress. The first term on the right-hand side of (26) is an unknown correlation between instant value of the interfacial force density (Drew, 1983) $((p-p_{\mathrm{i}})\mathbf{I}-\mathbf{T})\cdot\nabla\theta_k$ and velocity fluctuation. The second term on the right-hand side of (26) contains the unknown correlation between velocity fluctuation and dynamics of the interface expressed by the gradient of the indicator function. High-density ratio common to the most of bubbly flows and inequality (18) allows receiving a remarkably simple closure for the first term in (26). Assuming physically meaningful norm for Reynolds stress in (18) as

$$\left\|\mathbf{T}_k^{Re}\right\|=\rho_k k_k \tag{27}$$

inequality (18) becomes

$$\rho_{\mathrm{C}}k_{\mathrm{C}}\gg\rho_{\mathrm{D}}k_{\mathrm{D}}. \tag{28}$$

The conservation equation for the total turbulent kinetic energy of two-phase system is obtained by a summation of Eq. (24) for each phase. Due to inequality (28), all single-phase terms weighted by the gas density are negligible to the order $\mathrm{O}(\rho_{\mathrm{D}}/\rho_{\mathrm{C}})$. Thus, the total mixture turbulent kinetic energy balance becomes (Kataoka and Serizawa, 1989)

$$\frac{\partial(\rho_{\mathrm{C}}\alpha_{\mathrm{C}}k_{\mathrm{C}})}{\partial t}+\nabla\cdot(\rho_{\mathrm{C}}\alpha_{\mathrm{C}}\mathbf{U}_{\mathrm{C}}k_{\mathrm{C}})=\alpha_{\mathrm{C}}\mathbf{T}_{\mathrm{C}}^{Re}:(\nabla\mathbf{U}_{\mathrm{C}})$$
$$-\nabla\cdot\left(\frac{\rho_{\mathrm{C}}\langle\theta_{\mathrm{C}}\mathbf{U}_{\mathrm{C}}'\left|\mathbf{U}_{\mathrm{C}}'\right|^2\rangle}{2}+\langle\theta_{\mathrm{C}}\mathbf{U}_{\mathrm{C}}'P_{\mathrm{C}}'\rangle-\langle\theta_{\mathrm{C}}\mathbf{U}_{\mathrm{C}}'\cdot\mathbf{T}_{\mathrm{C}}'\rangle\right)-\rho_{\mathrm{C}}\alpha_{\mathrm{C}}\varepsilon_{\mathrm{C}}$$
$$+\sum_{k=\mathrm{C,D}}\langle((p-p_{\mathrm{i}})\mathbf{I}-\mathbf{T})\cdot\nabla\theta_k\cdot\mathbf{U}_k'\rangle$$
$$+\sum_{k=\mathrm{C,D}}((p_{\mathrm{i}}-P_k)\mathbf{I}+\mathbf{T}_k):\langle\mathbf{U}_k'\nabla\theta_k\rangle. \tag{29}$$

Using Eqs. (25) and (7) the first sum in the last line of Eq. (29) becomes

$$\sum_{k=\mathrm{C,D}} \left\langle ((p-p_\mathrm{i})\mathbf{I}-\mathbf{T})\cdot\nabla\theta_k\cdot\mathbf{U}'_k \right\rangle = \mathbf{U}_\mathrm{r}\cdot\mathbf{M}_\mathrm{C}. \tag{30}$$

A remarkable feature about (30) is that it is exact to the order $\mathrm{O}(\rho_\mathrm{D}/\rho_\mathrm{C})$ and does not require any further modeling. Thus, correlation between velocity fluctuation at the interface and interfacial force density for the two-phase mixture is exactly equal to the work of interfacial force density per unit time. Since typical bubbly flow is drag dominated, Eq. (30) becomes

$$\mathbf{U}_\mathrm{r}\cdot\mathbf{M}_\mathrm{C} = \frac{3}{4}\frac{C_\mathrm{d}}{d}\alpha_\mathrm{D}\rho_\mathrm{C}|\mathbf{U}_\mathrm{r}|^3 > 0. \tag{31}$$

Physically it is associated with the pseudoturbulence generated by the chaotic liquid displacement due to the bubbles. Small portion of energy defined in (31) contributes to the rotational part of liquid turbulence due to the vorticity generated by bubble wakes.

Remaining term to be modeled is the last sum of the right-hand side of Eq. (29). Kataoka and Serizawa (1989) assumed that fluctuating motion of interface is isotropic, i.e., $\langle\mathbf{U}'_k\nabla\theta_k\rangle = 0$. Further, interfacial pressure difference was neglected in the momentum equation. Thus, last interfacial term on the right-hand side of (29) was neglected.

Taking into account Eq. (31), the modeled form of the turbulent energy balance (29) becomes

$$\frac{\partial(\rho_\mathrm{C}\alpha_\mathrm{C}k_\mathrm{C})}{\partial t} + \nabla\cdot(\rho_\mathrm{C}\alpha_\mathrm{C}\mathbf{U}_\mathrm{C}k_\mathrm{C}) = \alpha_\mathrm{C}\mathbf{T}^{Re}_\mathrm{C} : (\nabla\mathbf{U}_\mathrm{C}) - \nabla \cdot\left(\frac{\rho_\mathrm{C}\nu^\mathrm{t}_\mathrm{C}}{Pr^\mathrm{KE}}\nabla k_\mathrm{C}\right) - \rho_\mathrm{C}\alpha_\mathrm{C}\varepsilon_\mathrm{C} + \frac{3}{4}\frac{C_\mathrm{d}}{d}\alpha_\mathrm{D}\rho_\mathrm{C}|\mathbf{U}_\mathrm{r}|^3, \tag{32}$$

where turbulent energy Prandtl number $Pr^\mathrm{KE} = 1.0$ in standard k–ε model (Launder and Spalding, 1974).

Turbulent kinetic energy balance (32) contains unknown dissipation rate defined in (23). Assuming isotropic turbulence, Eq. (23) reduces to

$$\varepsilon_k = \frac{\nu_k}{\alpha_k}(\langle\theta_k\nabla\mathbf{U}'_k : \nabla\mathbf{U}'_k\rangle). \tag{33}$$

Thus, a separate transport equation for the liquid dissipation rate defined in (33) is required. An exact transport equation for the single-phase dissipation rate contains third-order correlations, which must be modeled. In the k–ε approach, the modeled balance for ε is based on the Kolmogorov's hypothesis that the time scale of single-phase turbulence destruction is determined by the time scale of the smallest eddies responsible for dissipation. Thus, production and dissipation rates of dissipation rate are assumed proportional to the turbulence production and dissipation rates multiplied by the smallest eddy frequency scale ω. Dimensional analysis results in (Launder and Spalding, 1974)

$$\omega = \frac{\varepsilon}{k}. \tag{34}$$

Of course, such approach is nothing more but an exercise in scaling analysis. Therefore, the modeled form of the dissipation rate balance has very little in common with the original equation. Therefore, a consistent way to model interfacial terms in turbulence dissipation balance is to

adopt the same approach as it was done in the single-phase model. The interfacial term in dissipation rate equation is assumed to be proportional to the bubble-induced production term (31) multiplied by the characteristic frequency of bubble-induced pseudoturbulence destruction. Another fundamental question is whether single-phase turbulence destruction frequency defined in Eq. (34) is the characteristic frequency of bubble-induced turbulence destruction. Lopez de Bertodano (1992) considered decay of homogeneous two-phase turbulence. He found that if the single-phase frequency (34) were assumed as the time scale of bubble pseudoturbulence destruction, then the turbulence decay would depend on the initial dissipation rate. Such dependency is unphysical. A modified model of two-phase turbulence was proposed. Turbulence in the liquid phase was assumed to be a sum of shear and bubble-induced turbulence fields. Such superposition is valid for low-void fraction flows (Lance and Bataille, 1991). It can be viewed only as a first approximation of generally non-linear interaction. Based on the results of bubble-induced pseudoturbulence in the potential flow, Lopez de Bertodano (1992) proposed a new expression for the bubble pseudoturbulence dissipation frequency

$$\omega_{\mathrm{b}} = \left(\frac{2C_{\mathrm{vm}} d}{3C_{\mathrm{d}} |\mathbf{U}_{\mathrm{r}}|} \right)^{-1}. \tag{35}$$

Eq. (35) states that the characteristic time scale of bubble pseudoturbulence destruction is determined by the bubble residence time rather than smallest eddy time scale from (34). For typical bubbly flow $\omega_{\mathrm{b}} \gg \omega$, i.e., bubble pseudoturbulence decays much faster than shear-induced turbulence. Introduction of the second dissipation time scale leads to the correct asymptotic behavior of the model for homogeneous turbulence decay. Thus, an appropriate modeled form of the dissipation rate balance would be

$$\frac{\partial(\rho_{\mathrm{C}}\alpha_{\mathrm{C}}\varepsilon_{\mathrm{C}})}{\partial t} + \nabla\cdot(\rho_{\mathrm{C}}\alpha_{\mathrm{C}}\mathbf{U}_{\mathrm{C}}\varepsilon_{\mathrm{C}}) = \omega\left(C_1\alpha_{\mathrm{C}}\mathbf{T}_{\mathrm{C}}^{Re} : (\nabla\mathbf{U}_{\mathrm{C}}) - C_2\rho_{\mathrm{C}}\alpha_{\mathrm{C}}\varepsilon_{\mathrm{C}}\right) - \nabla\cdot\left(\frac{\rho_{\mathrm{C}}\nu_{\mathrm{C}}^{\mathrm{t}}}{Pr^{\mathrm{DR}}}\nabla\varepsilon_{\mathrm{C}}\right) + \omega_{\mathrm{b}}C_3\frac{3}{4}\frac{C_{\mathrm{d}}}{d}\alpha_{\mathrm{D}}\rho_{\mathrm{C}}|\mathbf{U}_{\mathrm{r}}|^3, \tag{36}$$

where $C_1 = 1.44$, $C_2 = 1.92$, $Pr^{\mathrm{DR}} = 1.272$ from the standard k–ε model (Launder and Spalding, 1974) and C_3 is a new unknown model constant.

Turbulent scalar balance equations (32) and (36) explicitly contain interfacial terms. In the single-phase limit, they correctly approach single-phase k–ε equations. The proposed model has the single empirical constant C_3. This constant is expected to be universal for incompressible turbulent adiabatic bubbly flows. Such universality will be assessed later by comparison of CFD predictions with experiment.

4. Wall boundary conditions

The single-phase k–ε turbulence model relies on the wall function (Launder and Spalding, 1974) approach as a wall boundary condition for high-Re number flows. Wall function is widely used in practical calculations because it avoids very fine grids needed to resolve turbulent boundary layer. It also seems attractive to utilize wall function in the two-phase turbulence model. The key

question is whether the continuous phase average velocity obeys the log law. Recent experiments give a positive answer. However, presence of bubbles in the boundary layer introduces corrections into the log law. Marié et al. (1997), Nakoryakov et al. (1981, 1996), and Sato et al. (1981) investigated the boundary layer of upward and downward turbulent air–water bubbly flows. It was found that the two-phase boundary layer has the same structure as its single-phase counterpart. It consists of viscous sublayer, log layer and outer flow region. Typical upward flow void fraction profile featured peak in the log layer. Liquid mean velocity profile in the log layer ($y_+ \cong 30$–200) was found to obey the logarithmic law

$$U_+ = \frac{1}{\kappa^{\mathrm{TP}}} \ln (y_+) + B^{\mathrm{TP}}, \tag{37}$$

where $U_+ = U_{\mathrm{C}}/U_{\mathrm{w}}^{\mathrm{TP}}$ is the normalized liquid tangential velocity, $y_+ = yU_{\mathrm{w}}^{\mathrm{TP}}/\nu_{\mathrm{C}}$ is the normalized wall normal distance, $U_{\mathrm{w}}^{\mathrm{TP}}$ is the two-phase frictional velocity defined as $U_{\mathrm{w}}^{\mathrm{TP}} = (\tau_{\mathrm{w}}^{\mathrm{TP}}/\rho_{\mathrm{C}})^{1/2}$, $\tau_{\mathrm{w}}^{\mathrm{TP}}$ is the two-phase wall shear stress exerted on liquid, κ^{TP} and B^{TP} are the two-phase Von Karman and additive constants, respectively. These constants were found functions of the flow parameters when bubbles were present in the boundary layer. Log law constants retained their single-phase values $B^{\mathrm{SP}}(\cong 5.45)$ and $\kappa^{\mathrm{SP}}(\cong 0.419)$ in bubbly flows with few or no bubbles in the boundary layer. Such situation was typical for the downward flows where lift force drove bubbles from the boundary layer.

Troshko and Hassan (2001) proposed a new logarithmic wall law for the turbulent bubbly boundary layer. They assumed that Couette type boundary layer assumptions are valid for the bubbly boundary layer as well. In this case, the momentum equation (6) reduces to

$$\alpha_{\mathrm{C}} \nu_{\mathrm{C}}^{\mathrm{t}} \frac{\partial U_{\mathrm{C}}}{\partial y} = U_{\mathrm{w}}^{\mathrm{TP}^2}, \tag{38}$$

where y is wall normal coordinate and U_{C} is tangential velocity. The main assumption was that liquid eddy diffusivity is a sum of the shear-induced component given by Von Karman mixing length hypothesis and the bubble-induced component. Bubble-induced eddy diffusivity was assumed to be a product of local slip velocity and wall normal distance as the mixing velocity scale and the length scale, respectively. An empirical function accounting for non-linearity of shear and bubble-induced turbulence interaction was introduced. The result was the logarithmic law expressed by (37), where

$$\kappa^{\mathrm{TP}} = \kappa^{\mathrm{SP}} \beta^{-1}, \tag{39}$$

$$B^{\mathrm{TP}} = y_+^0 \left(\beta^{-1} - 1\right) - \ln (\beta)/\kappa^{\mathrm{SP}}. \tag{40}$$

In Eqs. (39) and (40), a two-phase correction parameter β is determined by

$$\beta = \left[(1 - \alpha_{\max}) \left(1 + \frac{\kappa_1 \alpha_{\max} |\mathbf{U}_{\mathrm{r}}|}{\kappa^{\mathrm{SP}} U_{\mathrm{w}}^{\mathrm{TP}}} \right) \right]^{-1}, \tag{41}$$

where $y_+^0 \cong 11$ is the viscous sublayer thickness and $\alpha_{\max} = \max t(\alpha_{\mathrm{D}} | 12 < y_+ < 300)$ is the maximum void fraction in the boundary layer. Physically, $\alpha_{\max}$ is related to the probability of bubble presence. We deduced the empirical non-linearity function $\kappa_1 = 4.9453\mathrm{e}^{-40.661 U_{\mathrm{w}}^{\mathrm{TP}}}$ ($U_{\mathrm{w}}^{\mathrm{TP}}$ is in m/s) from the experimental data of Marié et al. (1997).

Based on Eqs. (37) and (38) and assumption of turbulence equilibrium in the bubbly boundary layer, the following boundary conditions were derived for the turbulent scales (Troshko and Hassan, 2001):

$$k_C = \frac{U_w^{TP^2}}{\sqrt{C_\mu}}, \tag{42}$$

$$\varepsilon_C = \frac{\beta U_w^{TP^3}}{\kappa^{SP} y} = \frac{U_w^{TP^3}}{\kappa^{TP} y}. \tag{43}$$

The boundary condition expressed by (43) differs from its single-phase counterpart. The difference is that the two-phase dissipation time scale is reciprocal to β, i.e., it is determined by not only velocity scale U_w^{TP} and length scale y, but also two-phase parameters contained within β.

5. Numerical solution technique

The mathematical model developed above consists of continuity equation (5), momentum equation (6), turbulent energy balance (32) and dissipation rate balance (36). These equations are complimented by the wall boundary conditions expressed by Eqs. (37)–(43) and total volume conservation $\alpha_C + \alpha_D = 1$. The mathematical complexity of the model warrants numerical solution as the only practical option. The CFX4.2 program was used for the numerical integration.

CFX4.2 (AEA Technology, 1997) is a commercial suit of CFD software with multi-phase capabilities. Computational grid is based on the unstructured set of blocks each containing structured grid. The structured grid within each block is generated using general curvilinear coordinates ensuring accurate representation of the flow boundaries. Discretization of the partial differential equations is based on the conservative finite volume method (FVM). Non-staggered grid is employed where all primitive variables are stored in the geometrical centers of control volumes. The program is able to handle all non-drag interfacial forces. The non-drag force coefficients can be supplied by the user. The drag coefficient was calculated in the following way. First, three drag coefficients are calculated based on the various flow regimes. These regimes and corresponding drag coefficient expressions are shown in Table 1. In this table, Eotvos number is a dimensionless ratio between buoyancy and surface tension force expressed by the surface tension coefficient σ

$$Eo = \frac{|\mathbf{g}|(\rho_C - \rho_D)d^2}{\sigma}. \tag{44}$$

All drag coefficients could be modified to account for the bubble concentration effect according to Ishii and Zuber (1979). Then, an appropriate drag coefficient is chosen based on the following

Table 1
Drag coefficient regimes

Drag regime	Drag coefficient
Viscous, $0 < Re_b < 500 \rightarrow 1000$	$C_d^v = 24(1 + 0.1Re_b^{0.75})/Re_b$
Inertial, $500 \rightarrow 1000 < Re_b < 10^5$	$C_d^i = 2Eo^{1/2}/3$
Spherical cap (large bubbles)	$C_d^s = 8/3$

criterion. The viscous regime is adopted if it is greater than the inertial drag. Otherwise, it is a minimum of the inertial and the spherical cap drag coefficients (AEA Technology, 1997). Two-phase version of SIMPLEC algorithm (AEA Technology, 1997) was used for pressure–velocity coupling. Discretized momentum equations were solved by the Stone's method, turbulent scalars by the line underelaxation method and pressure by the algebraic multi-grid method (AEA Technology, 1997).

The model was implemented in CFX4.2 program via user defined FORTRAN subroutines. Interfacial terms in (32) and (36) were added to the discretized turbulence equations with user-defined constant C_3. Another routine was used to implement the new wall law (37)–(42). Due to the limitation on the user introduced modifications, the two-phase boundary condition for dissipation rate (43) could not be implemented. This implies that the boundary condition (43) was implemented with $\beta = 1$. This led to a lower calculated turbulent energy. However, as it is indicated in (42) $U_w^{TP} \propto \sqrt{k_C}$, thus the effect of such inconsistency should not affect friction velocity. Nevertheless, a correction coefficient C_τ was introduced in calculation of shear stress to account for this deficiency. Since wall friction is proportional to the turbulence level in the boundary layer, it is expected that $C_\tau \geqslant 1$.

Total numerical error arises from several sources (Ferziger, 1993), discretization error, iteration non-convergence error, and far boundary error. Discretization error can be estimated from the grid refinement studies. This study may be computationally costly. However, log law of the wall utilized in the present model requires that the first computational node to be located at least 12 wall length units from the wall. This requirement sets a limit on the systematic refinement study. Therefore, in all computations, grids were generated such that the first boundary node was located approximately 30 wall units from the wall. A grid refinement study was conducted for pipe bubbly flow and confirmed that "30 wall units" criterion is enough to achieve a grid independent solution (Troshko, 2000). In all numerical calculations presented below, diffusion terms and pressure were discretized by the central difference scheme, convective terms were discretized by the first-order upwind scheme (Hybrid scheme in momentum equation). Since we considered simple flows in the straight ducts, the flow path was coaligned with the grid lines. Thus, control calculations with higher-order upwind scheme for convective terms produced negligible change in results, i.e., under these conditions numerical diffusion was negligible. All calculations presented in the next section are steady-state solution because preliminary studies showed that time marching technique takes longer time to get a steady-state solution. Due to a strong interaction between phases, under relaxation factors in momentum equations were imposed by reducing the factors several times in comparison to the default values (AEA Technology, 1997). The iterative process was stopped when the sum of all control volume mass imbalances (integral mass error) of each phase was small fraction of the phasic inlet mass flow rate. This ensured that iteration non-convergence error was avoidable.

In all duct flow calculations presented in the next chapter, detailed inlet information was unavailable. Thus, flat inlet profiles were assumed for all variables. Values of inlet void fraction were calculated by area averaging of the experimental data. Having known superficial velocities, the inlet velocities for each phase were calculated. Inlet values of turbulent scalars were estimated based on hydraulic diameter and 2% liquid turbulence intensity. The outlet boundary condition assumed fully developed flow, i.e., axial gradients of all variables except pressure were set to zero. Such outlet condition ensures mass conservation. All obtained

numerical solutions were checked to make sure that the fully developed solution was indeed obtained.

6. Validation

Validation of the implemented model was accomplished by comparison of its predictions against available experimental data. Before validation, the value of the unknown model coefficient C_3 had to be estimated. It is relevant to recall, that in the standard k–ε model (Launder and Spalding, 1974), the value of coefficient C_2 was deduced from fitting model prediction of homogeneous decaying grid turbulence into experimental data. The value of Pr^{DR} was calculated from the boundary layer analysis as a function of C_μ, C_1, C_2 and κ^{SP}. Yet, the value of C_1 was deduced from the comparison of model prediction against free shear flow experiments, i.e., numerically tuned. Since both C_1 and C_3 are production term coefficients in ε equation, it is reasonable to deduce C_3 by numerical tuning too. Like in case with C_1, the choosing criterion for C_3 was the best agreement with experiment.

Bubbly vertical pipe flow experiments by Wang et al. (1987), Serizawa et al. (1975) and Liu (1998) were chosen for validation. In all experiments, adiabatic, incompressible, air–water bubbly flows at atmospheric pressure and room temperature were studied. Tables 2–4 lay out the global flow conditions for each experiment, where J denotes superficial velocity and overbar sign denotes the flow area average.

As it was shown by Wang et al. (1987), the lateral void distribution is governed by the non-drag forces and liquid turbulence. The non-drag force coefficients are the major source of uncertainty

Table 2
Global flow conditions of Wang et al. experiment used in validation (I.D. 57.15 mm pipe flow)

Case id	J_C^{in} (m/s)	J_D^{in} (m/s)	$\overline{\alpha_D}$[a]	$\overline{d}$ (mm)	Flow direction
W0	0.43	0	–	–	–
W1	0.43	0.1	0.132	2.8	Up
W2	0.43	0.27	0.310	3.0	Up
W3	0.43	0.4	0.383	3.2	Up
W4	0.71	0.1	0.145	2.8	Down
W5	0.71	0.27	0.288	3.0	Down
W6	0.71	0.4	0.371	3.2	Down
W7	0.71	0	–	–	–

[a] Average inlet void fraction was obtained from fully developed profile integration.

Table 3
Global flow conditions of Serizawa et al. Experiment used in validation (I.D. 60 mm upward pipe flow)

Case id	J_C^{in} (m/s)	J_D^{in} (m/s)	$\overline{\alpha_D}$	$\overline{d}$ (mm)
S0	1.03	0	–	–
S1	1.03	0.0753	0.0397	4.0
S2	1.03	0.151	0.1023	4.0
S3	1.03	0.302	0.1627	4.0

Table 4
Global flow conditions of Liu experiment used in validation (I.D. 57.2 mm upward pipe flow)

Case id	J_C^{in} (m/s)	J_D^{in} (m/s)	$\overline{\alpha_D}$	$\overline{d}$ (mm)
L1	0.5	0.1	0.12	9.87
L2	0.5	0.1	0.13	8.4
L3	0.5	0.1	0.15	4.18
L4	0.5	0.1	0.151	3.19
L5	0.5	0.1	0.151	2.94
L6	1.0	0.1	0.087	6.6
L7	1.0	0.1	0.095	3.7
L8	1.0	0.1	0.106	2.81
L9	1.0	0.4	0.23	13.36
L10	1.0	0.4	0.24	7.09
L11	1.0	0.4	0.25	4.85

Table 5
Non-drag force coefficients

	C_l	$-C_{w1}$	C_{w2}	C_{td}	C_p
Present work	0.06	0.02–0.03	0.04–0.06	0.01–0.03	0
Lopez de Bertodano	0.1	0.2	0.12	0.1	1.0
Morel	0.5	0	0	0.01–0.1	0

in two-fluid formulation. Therefore, before validation of the turbulence model, representative values of non-drag force coefficients were found by comparison to experimental data of Sato et al. (1981) (see Troshko (2000) for more details). Table 5 shows the comparison of our values to those found by Lopez de Bertodano (1992) and Morel (1997). As shown, the values of the coefficients vary considerably from author to author. Such discrepancy underlines an inherent weakness of the attempt to represent a complex interfacial momentum transfer by the linear superposition of several simple forces. For example, Lopez de Bertodano used the interfacial pressure difference force given by Eq. (15) with $C_p = 1.0$, which was neglected by Morel and us. However, the void fraction profiles predicted by the present model and the model of Lopez de Bertodano were very close.

It was also found (Lopez de Bertodano, 1992; Morel, 1997; Troshko, 2000) that for bubble diameter larger than 5 mm, the lift force becomes much weaker. In fact, $C_l = 0$ seems to be a good choice for such bubbles, which confirms the experimental trend observed by Moraga et al. (1999).

Experiment W1 of Wang et al. (1987) was used to estimate the model constant C_3. The nodalization scheme consisted of axisymmetric, uniform grid of 400 (axial direction) by 25 (radial direction) cells. Axial grid length was 175 pipe diameters. Fig. 1 shows that the void fraction radial profile was well predicted by our model and model of Lopez de Bertodano (1992), who used PHOENICS computer program to implement his model. In the figures presented here, x, r and R denote axial, radial coordinate and pipe radius, respectively. Figs. 2–4 display predicted off-diagonal (shear) Reynolds shear stress T_{Cxr}^{Re}/ρ_C, liquid velocity and turbulence intensity $(T_{Cxx}^{Re}/\rho_C)^{1/2}$. Predictions of Lopez de Bertodano (1992) were also included in the figures for comparison. Measured radial Reynolds shear-stress profile indicates that single-phase turbulence dominated

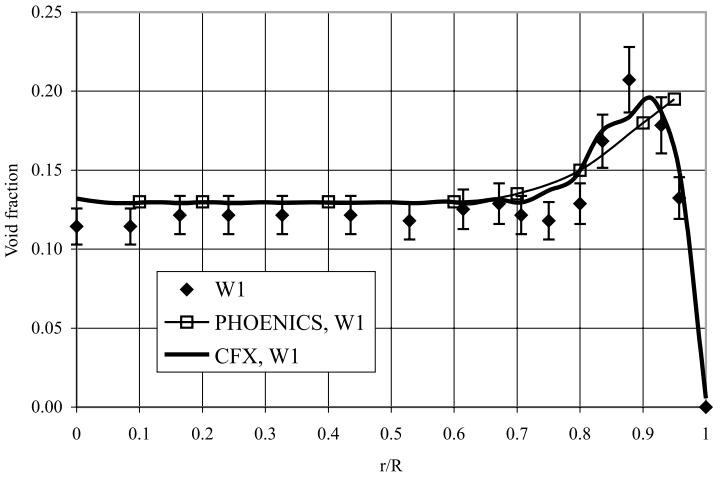

Fig. 1. Experiment W1. Void fraction comparison, $C_3 = 0.45$.

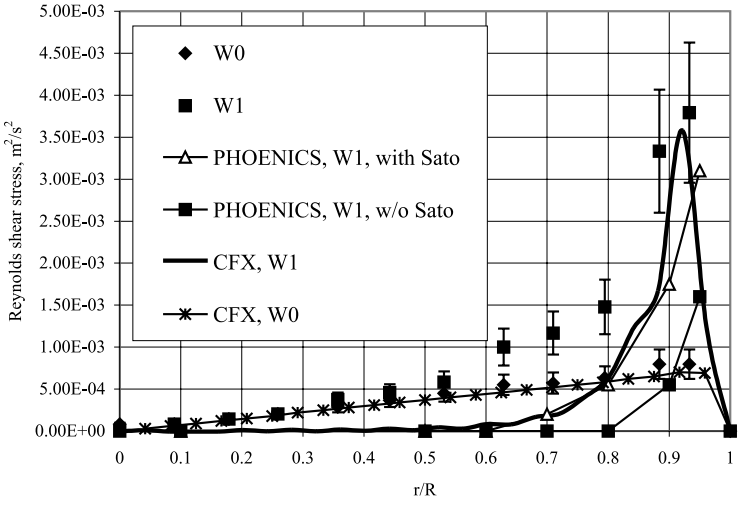

Fig. 2. Experiment W1. Reynolds shear-stress comparison, $C_3 = 0.45$.

the central half of the pipe, while bubble pseudoturbulence dominated the wall region, causing a sharp peak in T^{Re}_{Cxr}/ρ_C coinciding with the location of the void fraction maximum. According to our model,

$$T^{Re}_{Cxr} = \rho_C C_\mu \frac{k_C^2}{\varepsilon_C} \frac{\partial U_C}{\partial r} \tag{45}$$

in the fully developed regime, as it will be shown later, bubbles diminish velocity gradient. Therefore, the way our model could account for the increase of T^{Re}_{Cxr} is by increasing the turbulent viscosity associated with interfacial terms in Eqs. (32) and (36). Since interfacial term in (32) is

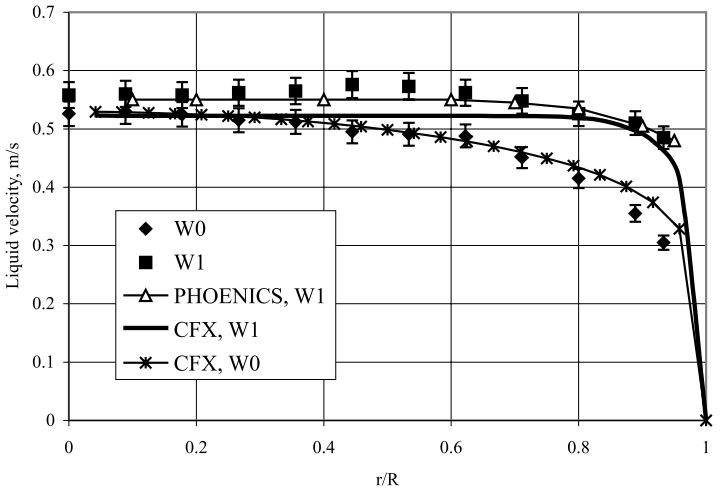

Fig. 3. Experiment W1. Liquid velocity comparison, $C_3 = 0.45$.

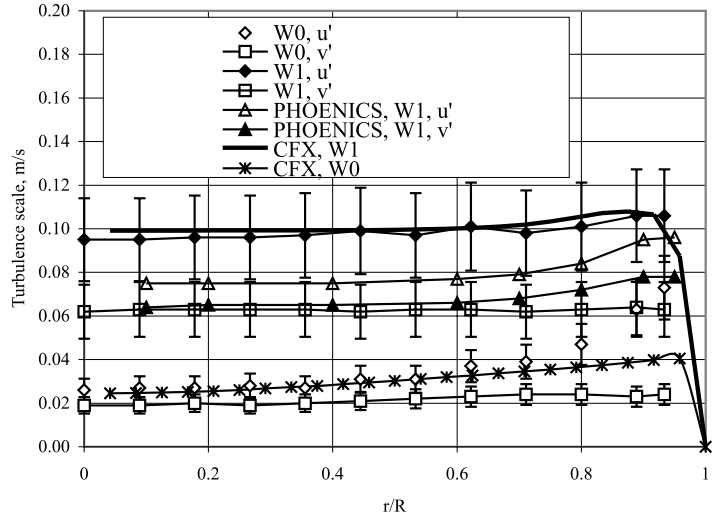

Fig. 4. Experiment W1. Comparison of r.m.s. liquid velocity, $C_3 = 0.45$.

exact, coefficient C_3 is the only free parameter quantifying the influence of bubbles on dissipation rate. Since the interfacial term in (36) is positive, a decrease of C_3 causes ε_C to decrease, too. According to (45), it leads to an increase of T^{Re}_{Cxr}. Therefore, the measured magnitude of Reynolds shear peak was a calibration parameter to tune the value of C_3. It was found that $C_3 \cong 0.45$ produced a favorable agreement with the data. Our model underpredicted the turbulence level in the central shear dominated region. Reynolds shear stress predicted by current model was close to the Lopez de Bertodano's calculation with bubble-induced eddy diffusivity of Sato et al. (1981). Calculation of Lopez de Bertodano without additional diffusivity underestimated the bubble-induced turbulence enhancement in the near wall region. Comparison of the liquid velocity profile

shows that both the present and Lopez de Bertodano's model correctly predicted the flattening of liquid velocity caused by the additional bubble induced mixing. Eddy diffusivity hypothesis assumes that the isotropic turbulent velocity scale (turbulence intensity) equal to $(2k_C/3)^{1/2}$. As shown in Fig. 4, the predicted turbulence intensity was in a good agreement with experiments. The model of Lopez de Bertodano showed also a reasonable agreement.

Experiments W2 and W3 were used to further check the universality of constant $C_3 = 0.45$ for the higher gas flow rate conditions. The computational grid used in the calculation was similar as in W1 case. Figs. 5–12 display the results of comparison. The predicted void fraction profiles

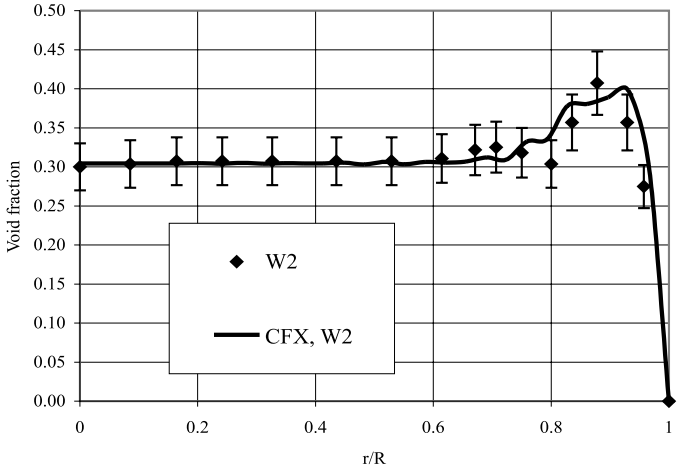

Fig. 5. Experiment W2. Void fraction comparison, $C_3 = 0.45$.

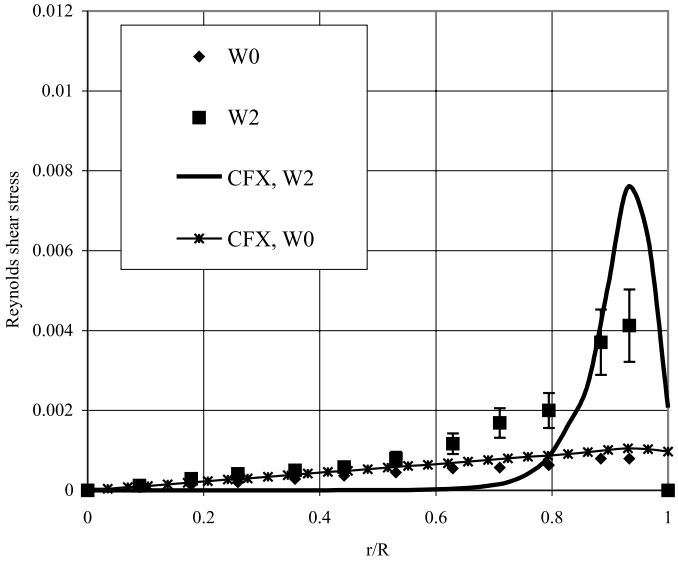

Fig. 6. Experiment W2. Reynolds shear-stress comparison, $C_3 = 0.45$.

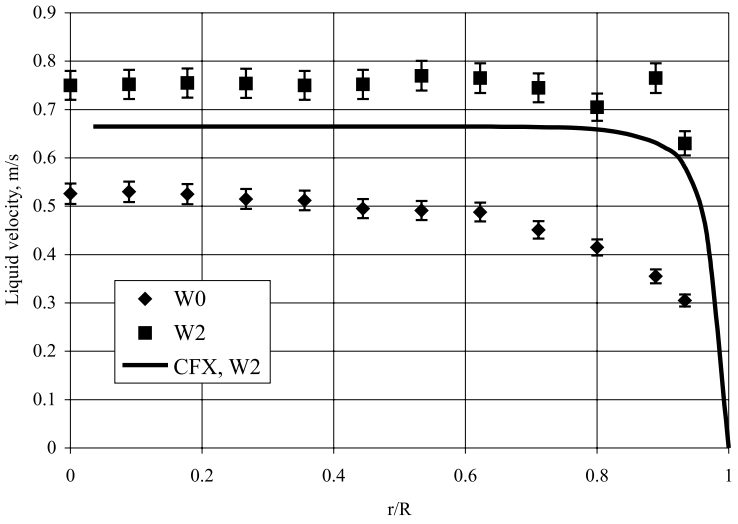

Fig. 7. Experiment W2. Liquid velocity comparison $C_3 = 0.45$.

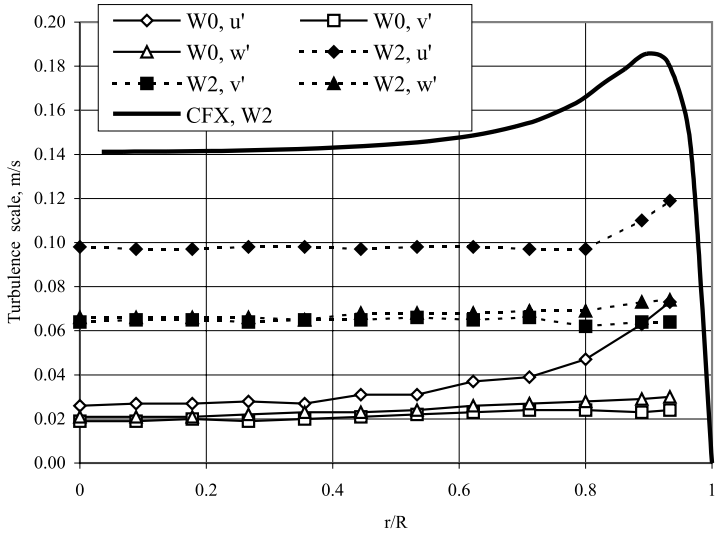

Fig. 8. Experiment W2. Comparison of r.m.s. liquid velocity, $C_3 = 0.45$.

agreed well with experimental data for both W2 and W3 experiments as shown in Figs. 5 and 9, respectively. Our model overestimated the stress magnitude in the bubble-dominated region for W2 case while good agreement was achieved for W3 as shown in Figs. 6 and 10. The model of Lopez de Bertodano overestimated the near wall shear stress with Sato viscosity. Our model overpredicted turbulence intensity for W2 and W3 (Figs. 8 and 12). Liquid velocity was well predicted by both models as illustrated in Figs. 7 and 11.

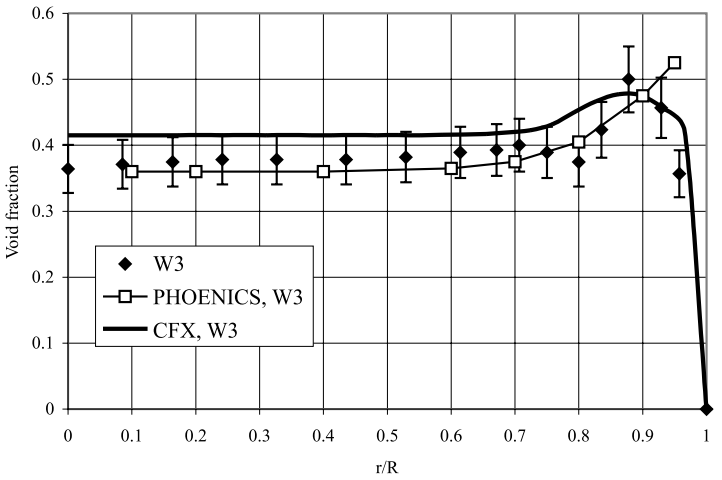

Fig. 9. Experiment W3. Void fraction comparison, $C_3 = 0.45$.

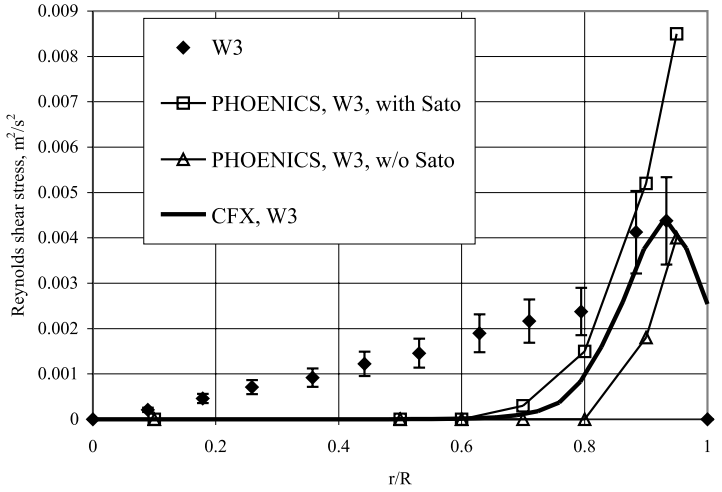

Fig. 10. Experiment W3. Reynolds shear-stress comparison, $C_3 = 0.45$.

Therefore, the value of 0.45 for the constant C_3 produced a good quantitative description for shear turbulence in experiments W1 and W3 and overestimated its effect in experiment W2 by the factor of 2–2.5. Turbulence intensity was well predicted in W1, and overpredicted in W2 and W3. Void fraction and liquid velocity profiles were well predicted.

To understand the influence of various production mechanisms of liquid turbulence, the production terms in the turbulent energy balance (32) were calculated. Figs. 13 and 14 plot the radial profiles of the bubble and shear production terms, respectively. As shown in Fig. 13, the bubble-induced pseudoturbulence term increases with the gas flow rate. Its radial distribution is almost similar to the void fraction profile. This is because the calculated slip velocity profile was

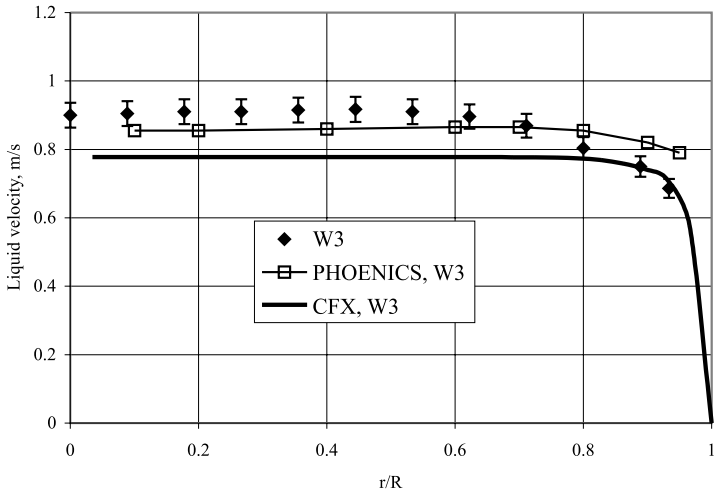

Fig. 11. Experiment W3. Liquid velocity comparison, $C_3 = 0.45$.

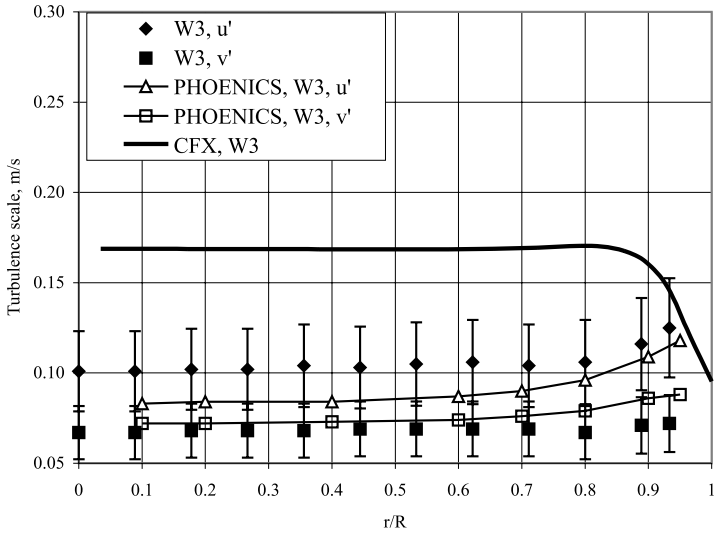

Fig. 12. Experiment W3. Comparison of r.m.s. liquid velocity, $C_3 = 0.45$.

essentially uniform. Fig. 14 indicates, that the shear production in cases W1 and W3 is lower than in the single-phase experiment W0. This is due to the effect of bubble-induced liquid velocity flattening. Thus, when bubbles are added to the liquid, the liquid turbulence modification is governed by two opposing mechanisms. On the one hand turbulence is augmented by the bubble-induced mixing, on the other hand shear turbulence is suppressed by the liquid velocity gradient reduction. It is reasonable to assume that at high-liquid flow rate, second (suppression) mechanism may become dominant leading to the bubble-induced turbulence suppression. Such mech-

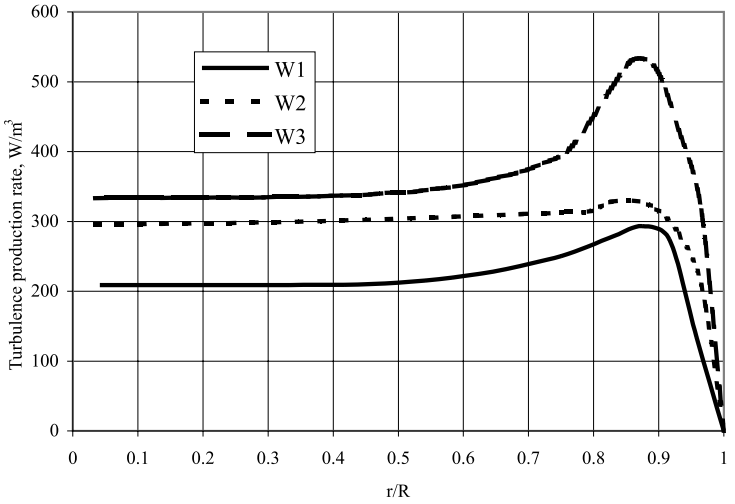

Fig. 13. Experiments W1–W3. Predicted bubble-induced turbulence production rate in (32).

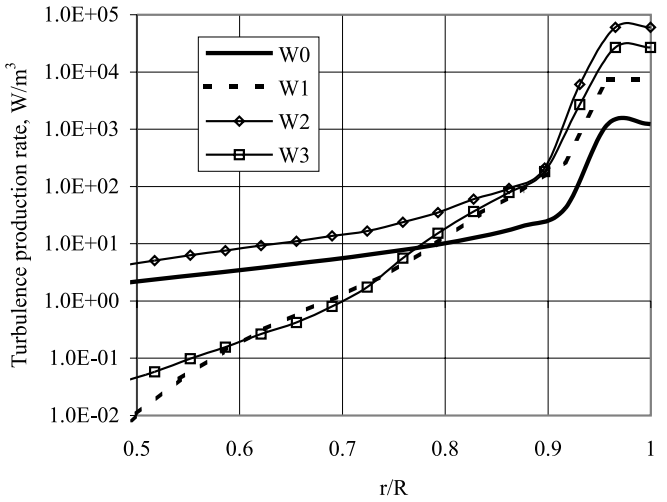

Fig. 14. Experiments W1–W3. Predicted mean shear-induced turbulence production rate in (32).

anism of bubble causing turbulence dissipation was explained by Lopez de Bertodano (1992). Indeed, this phenomenon was observed in experiments conducted by Serizawa et al. (1975) and Wang et al. (1987). Fig. 15 depicts the eddy diffusivity profile. As the gas flow rate increases, eddy diffusivity increases and its maximum shifts to the area where bubble-induced mixing is dominant. Fig. 15 also shows that eddy diffusivity for flow W2 was abnormally high, which led to the overestimation of turbulent shear stress.

To validate the model's ability to simulate downward flows, predictions of flows W4–W6 conditions were compared to experiments. Axisymmetric uniform grid consisted of 400 (axial)

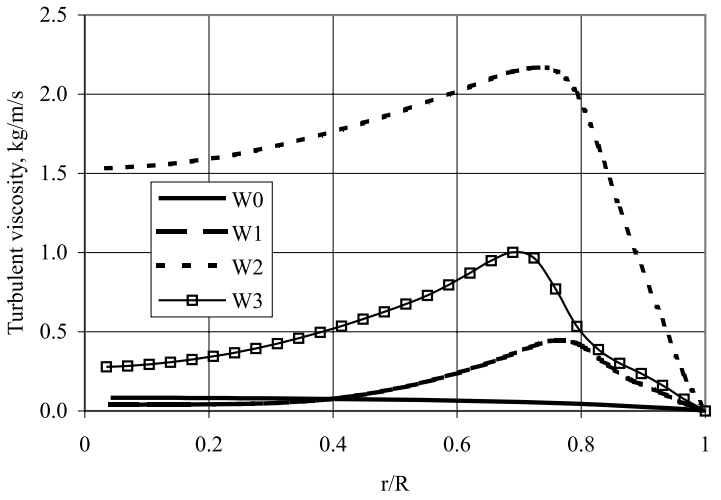

Fig. 15. Experiments W1–W3. Predicted turbulent viscosity.

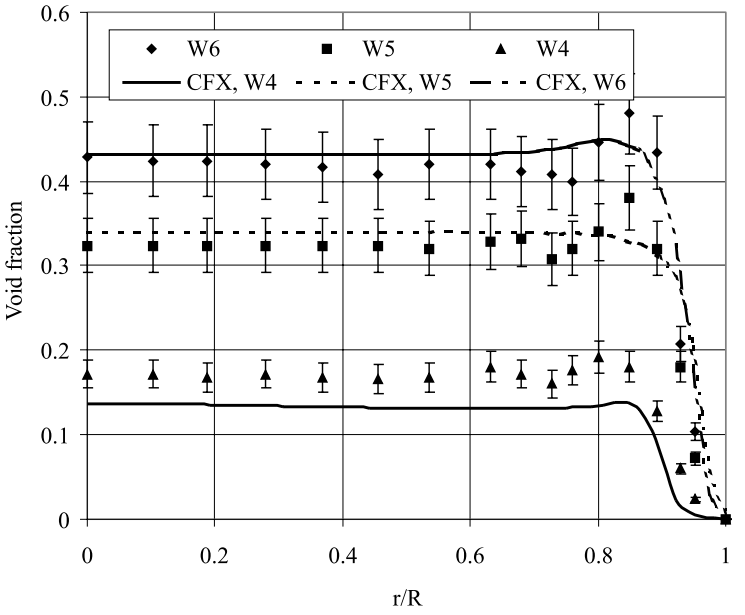

Fig. 16. Experiments W4–W7. Void fraction comparison.

by 40 (radial) cells was utilized. Axial grid length was 175 pipe diameters. Figs. 16–18 show the comparison for void fraction, liquid velocity and Reynolds shear stress. In downward flows, the lift force drives bubbles towards the pipe center (Wang et al., 1987). This results in void fraction maximum located along the pipe center. Downward flow liquid velocity has a maximum located off the pipe center. This phenomenon is referred to as "chimney" effect. As shown in Fig. 17,

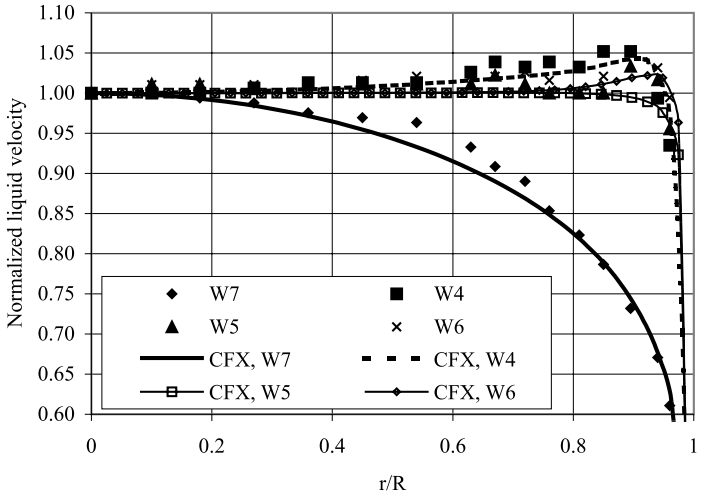

Fig. 17. Experiments W4–W7. Liquid velocity normalized by central line value.

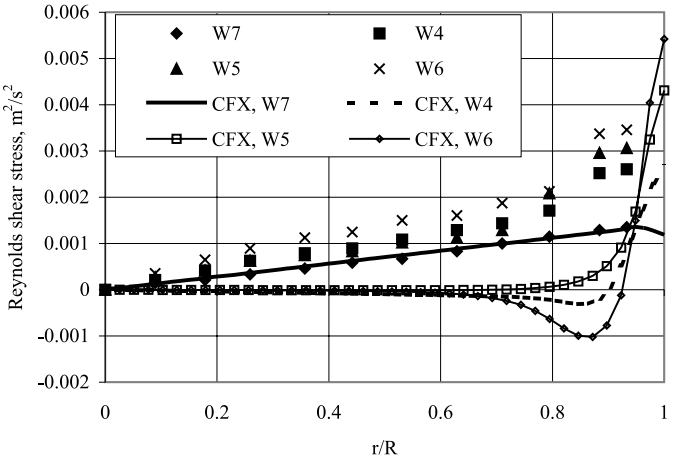

Fig. 18. Experiments W4–W7. Reynolds shear-stress comparison.

the predicted magnitude of off center velocity peak agrees with experiment. The existence of chimney effect in downward flows means that the liquid mean strain rate changes its sign in the fully developed regime. If eddy diffusivity hypothesis is valid, then Reynolds shear stress should too change the sign. However, Fig. 18 shows that the Reynolds shear-stress profile does not change its sign, contrary to predicted behavior. This means that Boussinesq hypothesis utilizing positive eddy diffusivity may not be valid to describe the turbulent field when chimney effect is present. More advanced turbulence models such as ASM or full Reynolds closure should be utilized.

The model was also checked against experiments S1–S3 of Serizawa et al. (1975). Axisymmetric uniform grid consisted of 400 (axial) by 40 (radial) cells was used in the computation. The axial

grid length was 83 pipe diameters. Figs. 19–21 display the void fraction comparison. As shown, a good agreement was achieved for the void fraction profiles in all conditions of the experiment. Predicted S1 liquid velocity profile, plotted in Fig. 22, exhibited chimney effect contrary to the experiment. Predicted S2 and S3 profiles exhibited typical flattened shape. Predicted bubble ve-

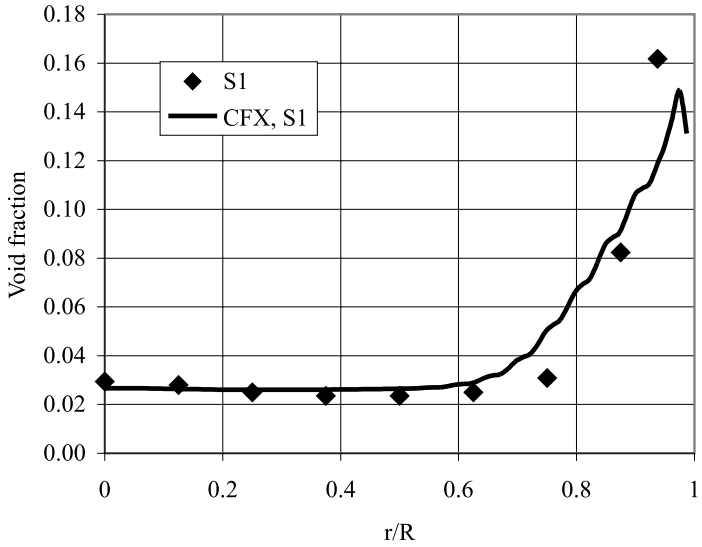

Fig. 19. Experiment S1. Void fraction comparison.

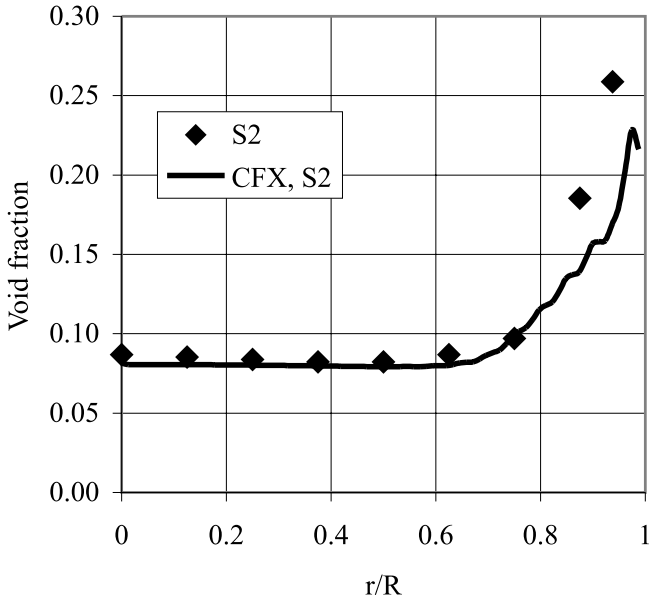

Fig. 20. Experiment S2. Void fraction comparison.

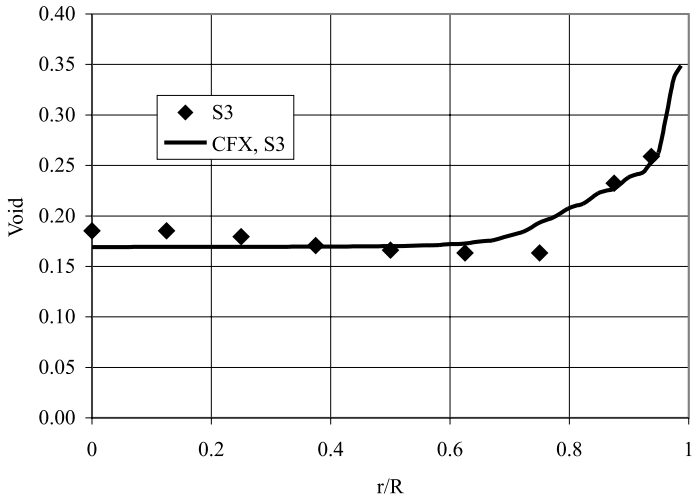

Fig. 21. Experiment S3. Void fraction comparison.

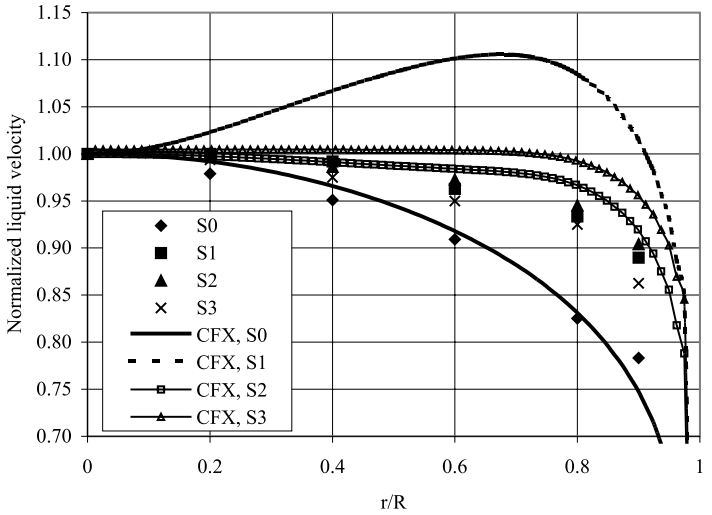

Fig. 22. Experiments S0–S3. Liquid velocity normalized by central line value.

locity profiles, shown in Fig. 23, had the same shape as its liquid counterparts due to the drag dominance. Figs. 24–26 display comparisons for the turbulence intensity. In experiments S1–S3 the shear-induced turbulence level was higher than in W1–W3 of Wang. This led to the bubble-induced turbulence suppression in S1 and S2 as evident from Figs. 24 and 25. Our model also predicted this effect for S1, while it slightly overestimated the turbulent scale for S2 and S3. Fig. 27 displays the slip velocity profile comparison. As shown, slip velocity exhibits maximum at the pipe center with significant reduction towards the wall. This is in contrary to the calculated profile, which is fairly uniform except small decline in the wall vicinity. Such behavior is more

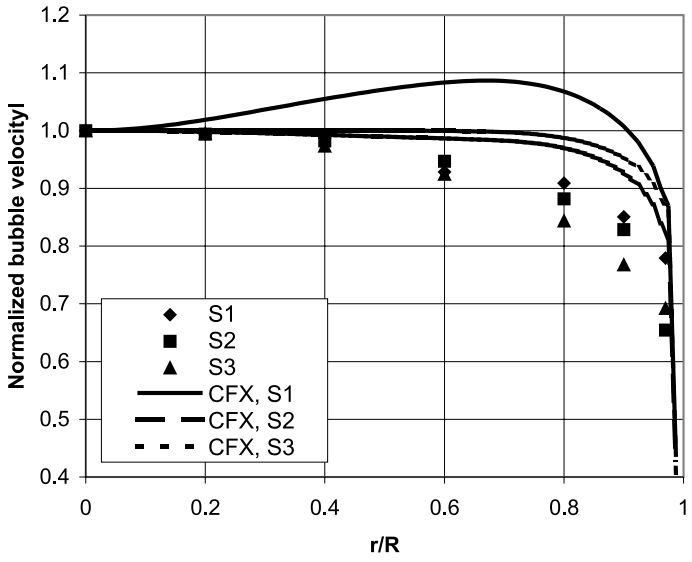

Fig. 23. Experiments S1–S3. Bubble velocity normalized by central line value.

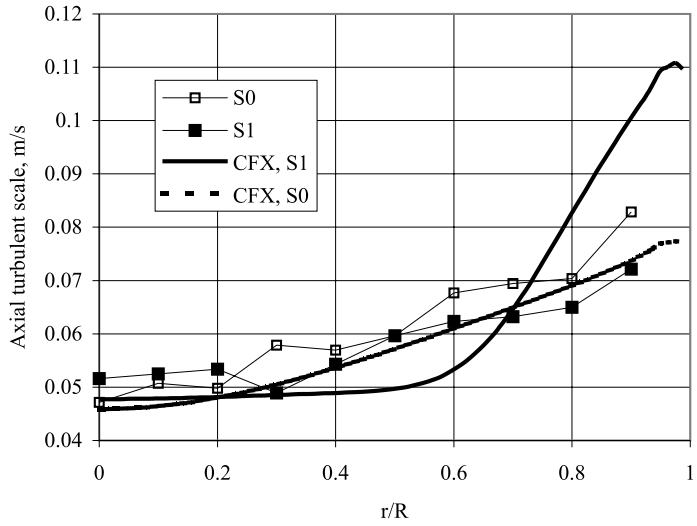

Fig. 24. Experiment S1. Comparison of r.m.s. liquid velocity.

characteristic for flows with non-uniform bubble size distribution. In fact, Serizawa et al. (1975) found that in all their experiments the bubble equivalent diameter had a normal distribution between 3.5 and 4 mm.

Experiments L1–L11 of Liu (1998) were used to validate the two-phase wall law (Troshko and Hassan, 2001). Liu found that bubbles with diameters larger than 5 mm exhibited the centerline peaked void fraction profile. Therefore, $\alpha_{max} \cong 0$ in Eq. (41) for such flows result into the single-

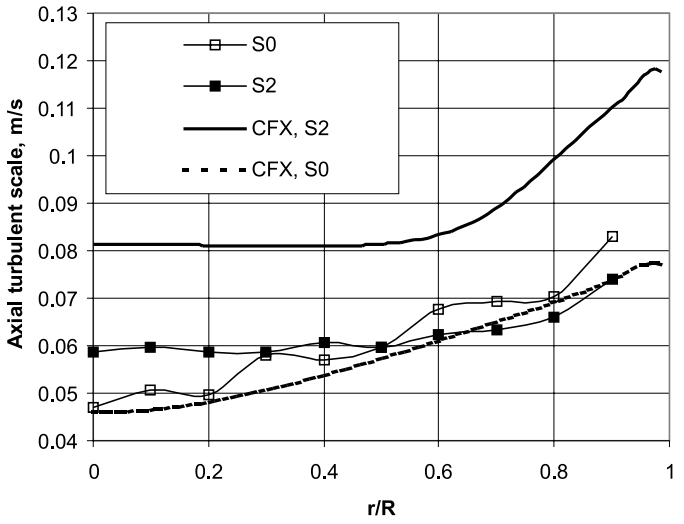

Fig. 25. Experiment S2. Comparison of r.m.s. liquid velocity.

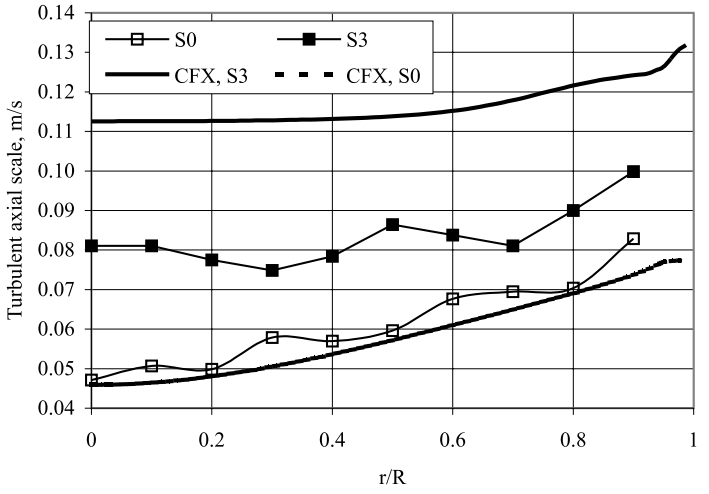

Fig. 26. Experiment S3. Comparison of r.m.s. liquid velocity.

phase wall law. For such experiments, the lift force was neglected and single-phase wall law was used. For flows with smaller, wall bound, bubbles, two calculations were performed: one with the conventional single-phase wall law and the other with the two-phase wall law. If the two-phase wall law was used, α_{max} in (41) was obtained from the experiment. For experiments L1–L5 correction factor of $C_\tau = 1.17$ was used. This value was deduced from the experiments of Sato et al. (1981) by Troshko (2000). No correction ($C_\tau = 1.0$) was used for L6–L11 experiments. In experiments L1–L5, an axisymmetric uniform grid consisted of 400 (axial) by 15 (radial direction) cells was utilized. Axial grid length was 88 pipe diameters. Figs. 28–30 show the comparison of

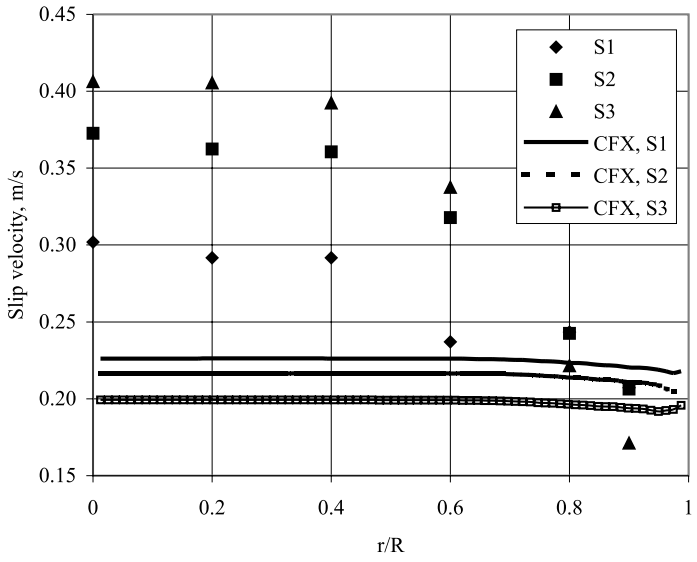

Fig. 27. Experiments S1–S3. Slip velocity comparison.

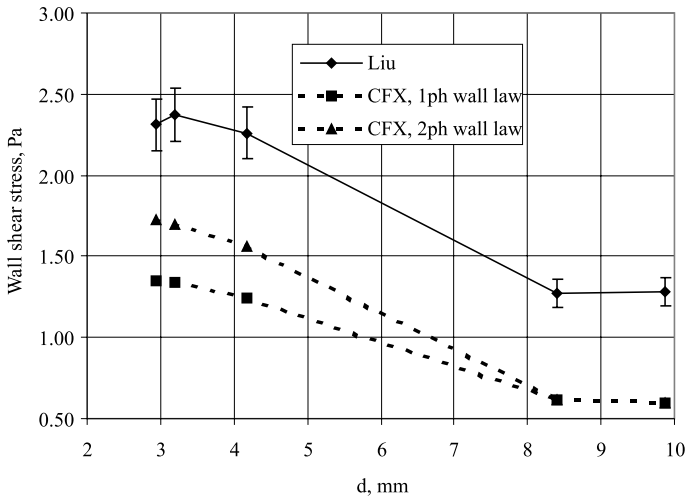

Fig. 28. Experiments L1–L5. Wall shear-stress comparison, $C_\tau = 1.17$.

predicted and experimental wall shear stress vs. bubble diameter. Eq. (41) indicates that the bubble-induced correction to the single-phase wall law is decreasing as the liquid flow rate is rising and the boundary layer void fraction decreasing. Thus, the largest difference between the single and two-phase wall law would be for the small bubble experiments L3–L5. Fig. 28 confirms this finding. As shown, the small bubble calculations with two-phase wall law predictions were in a better agreement with experiment. The model was also able to predict the effect of the wall friction reduction as the bubble size increases. As the bubble diameter gets bigger, the void fraction

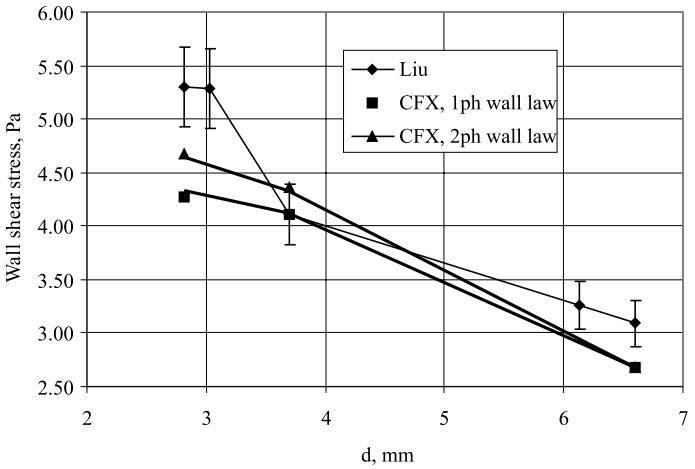

Fig. 29. Experiments L6–L8. Wall shear-stress comparison, $C_\tau = 1$.

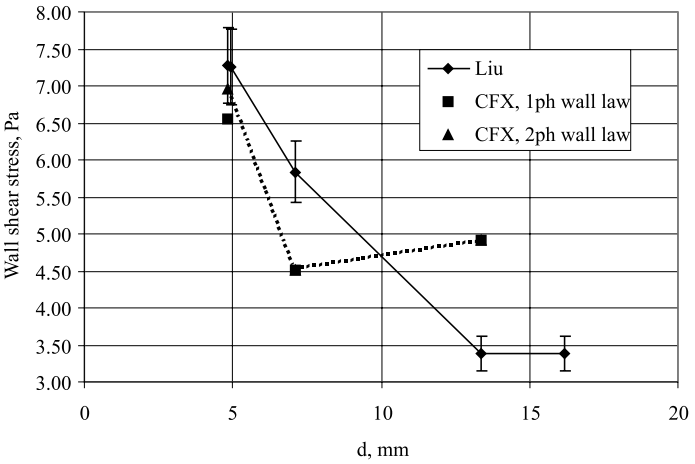

Fig. 30. Experiments L9–L11. Wall shear-stress comparison, $C_\tau = 1$.

maximum shifts further from the wall. This shift causes the boundary layer liquid velocity gradient in to decrease resulting in the friction reduction.

The ability of the model to predict the bubble size effect is illustrated in Figs. 31–34. As shown, the predicted void profiles in the near wall region agreed well to experiment for the small bubbles (2.81 and 3.7 mm). Void fraction in the core region was underpredicted. Such disagreement does not seem to be due to the bubble size non-uniformity because Fig. 34 shows that small bubbles had almost uniform size. Other reason might be that the flow was not fully developed because measured small bubble void profile did not exhibit axial symmetry as shown in Fig. 31. Predicted large bubble (6.6 mm) void profile was in reasonable agreement with experiment in the core region. However, in the near wall region, void fraction was underpredicted. In this case,

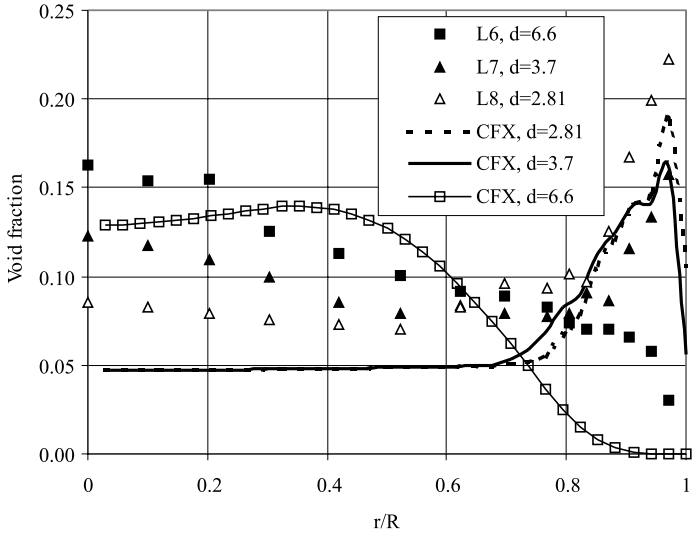

Fig. 31. Experiments L6–L8. Void fraction comparison.

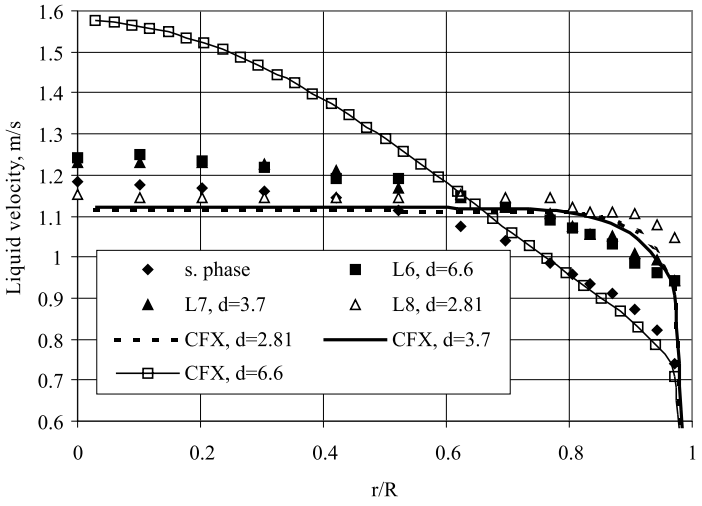

Fig. 32. Experiments L6–L8. Liquid velocity comparison.

disagreement seems to be due mainly to the bubble size non-uniformity because smaller size bubble dominated the wall vicinity as illustrated in Fig. 34. The model correctly predicted the same liquid velocity profile for 2.81 and 3.7 mm bubbles. Prediction for 6.6 mm bubble profile exhibited a laminar-like shape. Here, the difference between calculation and experiment can be attributed to the presence of small bubbles and its velocity flattening effect in the boundary layer. The model could not account for this effect. Fig. 34 provides also a good indication to the bubble-

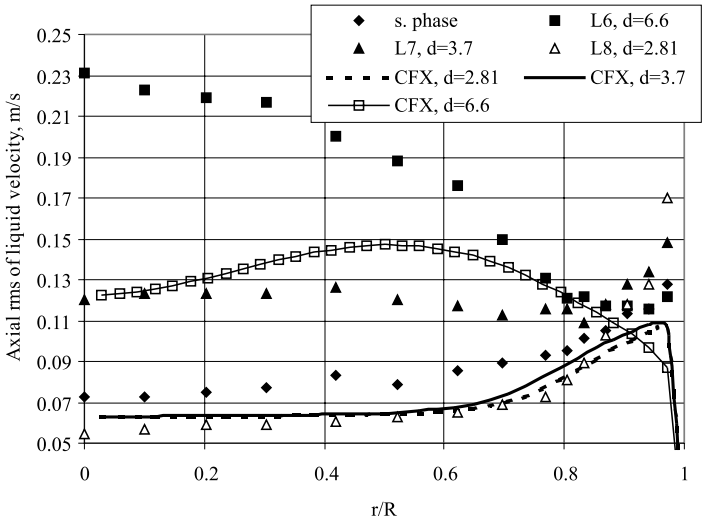

Fig. 33. Experiments L6–L8. Comparison of r.m.s. liquid velocity.

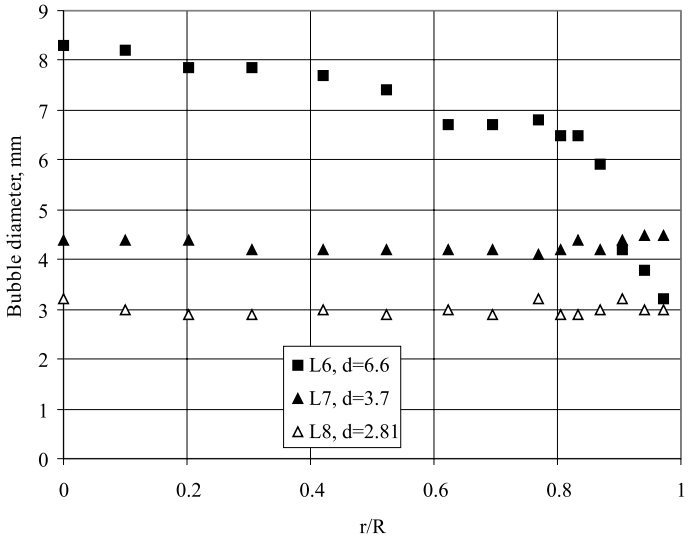

Fig. 34. Experiments L6–L8. Measured bubble diameter distribution, Liu (1998).

induced turbulence modification in liquid as discussed earlier. Small 2.81 mm bubbles suppressed turbulence by the mean strain rate reduction, while 3.7 and 6.6 mm bubbles produced enough mixing to promote turbulence. The model correctly predicted turbulence suppression due to the presence of 2.71 mm bubbles. However, it failed to predict turbulence promotion by 3.7 mm bubbles. It also correctly predicted the turbulence maximum shift from the wall vicinity to the free stream for 6.6 mm bubbles although turbulence intensity was underestimated.

Table 6
Global flow conditions of Lopez de Bertodano experiment used in validation (upward flow in triangular duct)

Case id	J_C^{in} (m/s)	J_D^{in} (m/s)	$\overline{\alpha_D}$	$\overline{d}$ (mm)
B0	1.0	0	–	–
B1	1.0	0.1	0.077	5.0

Vertical triangular duct experiment by Lopez de Bertodano (1992) was simulated to validate our model's performance in 3D case. Adiabatic, air–water fully developed bubbly flow at atmospheric pressure and room temperature was studied. Table 6 lays out the global flow conditions of the experiment. The cross-section of the duct was an isosceles triangle with 50 mm base and 100 mm height. The distance from the inlet to the measurement station was 73 hydraulic diameters ensuring fully developed flow.

The multi-block capability of CFX4.2 was used to create a 3D grid. The grid was 150 hydraulic diameters long. It had 200 cells in the axial direction and 300 cells in each lateral cross-section. The cells near triangle apex were skewed. Thus, computational results in this region may contain numerical errors.

Figs. 35–37 show comparisons for void fraction, axial mean velocity, and liquid Reynolds shear stress, respectively. It is necessary to note that Lopez de Bertodano (1992) used a circular sector to approximate the triangle cross-section by 400 nodes. The void fraction profile at the central line indicates that the lift force drove bubbles towards the wall resulting in the void peaks near the base and the apex walls. As shown in Fig. 35, the predicted void profile had some oscillations, especially noticeable in the apex region, which may be attributed to the poor grid quality in this zone. Liquid velocity comparison indicates velocity flattening by the bubbles is similar to the pipe flow. Lopez de Bertodano's prediction showed slightly better agreement for velocity predictions. Both Lopez de Bertodano and our calculation correctly predicted turbulence reduction in the

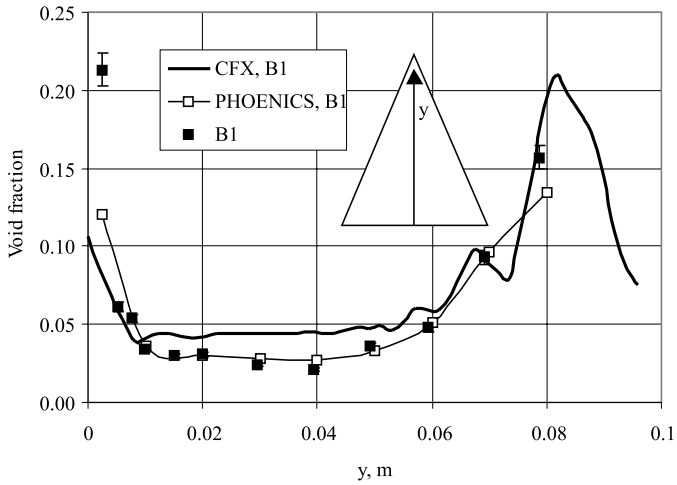

Fig. 35. Void fraction comparison, $z = 0$.

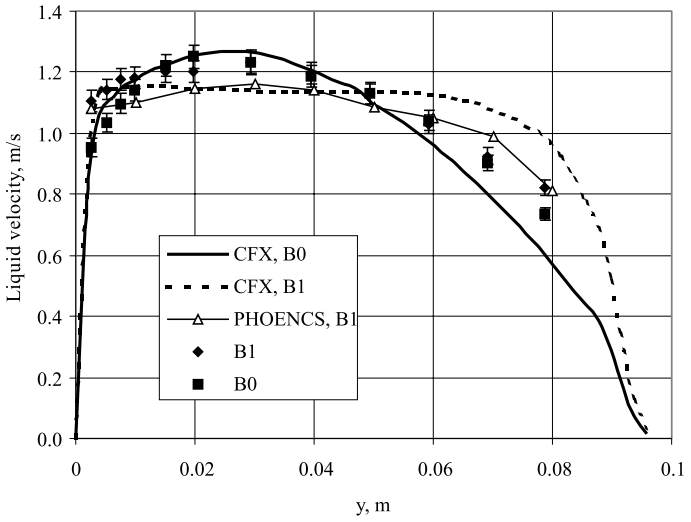

Fig. 36. Liquid velocity comparison, $z = 0$.

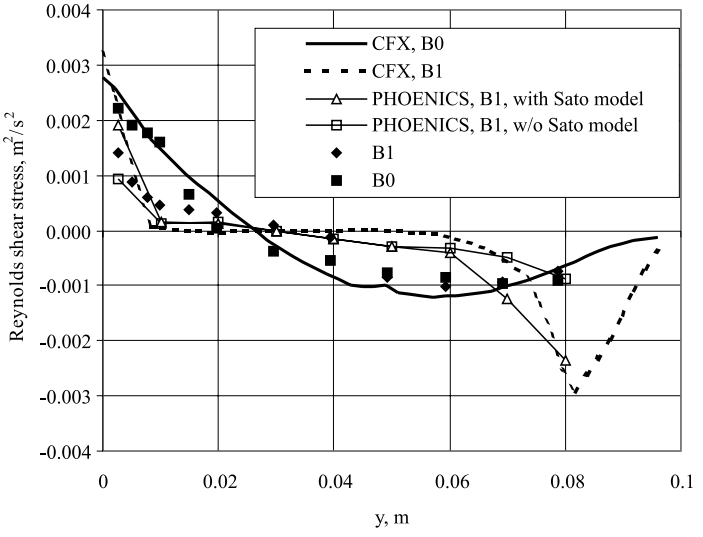

Fig. 37. Reynolds shear-stress comparison, $z = 0$.

region near the base wall. Model of Bertodano showed better agreement with the experiment without bubble-induced turbulence viscosity.

In conclusion, our model with empirical constants deduced from the 2D vertical pipe experiments showed a reasonable agreement with experiment in 3D case. Moreover, it compared well to the model of Lopez de Bertodano (1992) who employed more computationally expensive ASM and used finer grid.

7. Conclusions

In this research, a two-fluid, multi-dimensional model of turbulent bubbly flows was implemented in the CFD computer program and validated against available experimental data and predictions of the model by Lopez de Bertodano (1992).

To model turbulence in the liquid phase, a two-phase variant of k–ε model was used. The formulation of turbulent kinetic energy balance was based on the exact equation governing transport of total turbulent energy of two-phase mixture. This equation contained single-phase and interfacial terms. The single-phase terms were modeled via standard single-phase k–ε closure. The interfacial term was modeled based on the assumption of low-bubble inertia, which is valid for most bubbly flows. Physically, the interfacial term accounts for the additional turbulence production caused by the bubble induced mixing. Another important characteristic of liquid turbulence is turbulence dissipation rate. Standard k–ε closure was used to model its single-phase part. Effect of bubbles on the dissipation rate balance was modeled as the bubble-induced turbulent energy production multiplied by the characteristic frequency of bubble-induced turbulence dissipation. Based on the work of Lopez de Bertodano (1992) this frequency was estimated by the bubble residence time rather than time scale of smallest eddies.

A new two-phase wall law (Troshko and Hassan, 2001) was also utilized to serve as computationally inexpensive boundary condition. The derivation of the law was based on the assumption of additional turbulent viscosity accounting for bubble mixing in the boundary layer. The result was a logarithmic law where the law constants were functions of the flow parameters.

The model contained unknown empirical coefficient C_3 in the interfacial term of dissipation rate balance equation (36). This coefficient was numerically tuned by comparison of 2D numerical predictions against experiment of Wang et al. (1987) where bubble-induced turbulence was significant. The magnitude of the bubble-induced near wall peak in the Reynolds stress shear component served as calibration parameter. Numerical tuning showed, that $C_3 \cong 0.45$ is the best-fit value. To check the universality of this number, other 2D pipe and 3D triangular duct flows were simulated. It was shown that $C_3 \cong 0.45$ produces a good agreement for the Reynolds shear components. However, the predicted turbulence intensity was higher than experiment. This indicates that estimated value of interfacial turbulence coefficient $C_3 = 0.45$ possesses a certain generality. It was found that for some downward bubbly flows, the liquid Reynolds stress is not coaligned with the mean strain rate, so turbulent viscosity model is not applicable to such cases. The model was also able to capture bubble-induced turbulence suppression. It was shown that, indeed, this effect is due to the bubble-induced reduction of the mean shear production term in the turbulent kinetic energy balance relation. Our model also compared favorably with more computationally expensive ASM of Lopez de Bertodano.

Correct prediction of two-phase wall shear stress by mechanistic CFD model is very desirable since the knowledge of wall friction is important in engineering practice. The two-phase wall law has shown an improved agreement over conventional single-phase law. The improvement was especially noticeable for the low-Re number flows with small bubbles within boundary layers. The model was able to account for the bubble size effect on the wall friction under the same liquid and gas flow rate conditions.

In conclusion, our two-phase model of turbulence was found to describe well upward turbulent bubbly flows in straight ducts. It can serve as a basis for the development of more general models. The model described above is based on the eddy diffusivity models of turbulence. Such models do not take into account many important aspects of turbulence such as anisotropy. In gravity dominated bubbly flows, the instant relative velocity is predominantly aligned with the gravity vector. Therefore, a chaotic bubble motion will selectively enhance the gravity aligned component of liquid velocity fluctuation vector as observed by Wang et al. (1987). This may be a reason of generally poor prediction of turbulence scale by current model. Perhaps next step in this direction might be derivation of the exact conservation equation for two-phase Reynolds stress. With such improvements, the resulting model is expected to possess considerable predictive capability for a wide variety of turbulent gas–liquid dispersed flows.

References

AEA Technology, 1997. CFX4.2: Solver, Didcot, Oxfordshire, UK.

Drew, D.A., 1983. Mathematical modeling of two-phase flow. Ann. Rev. Fluid Mech. 15, 261–291.

Ferziger, J.H., 1993. Estimation and reduction of numerical error. In: Celik, I., Chen, C.J., Roache, P.J., Scheuerer, G. (Eds.), Symposium on Quantification of Uncertainty in Computational Fluid Dynamics, ASME FED Vol. 158. ASME FED Summer Meeting, Washington DC, June 20–24, pp. 1–8.

Ishii, M., Zuber, N., 1979. Drag coefficient and relative velocity in bubbly, droplet or particulate flows. AIChE J. 25, 843–856.

Kashiwa, B.A., Gore, R.A., 1991. A four equation model for multi-phase turbulent flow. In: Symposium on Turbulence Modification in Multiphase flows. Proceedings ASME-JSME Conference, Portland, Oregon, June 1999, pp. 23–27.

Kataoka, I., 1986. Local instant formulation of two-phase flow. Int. J. Multiphase Flow 12 (5), 745–758.

Kataoka, I., Serizawa, A., 1989. Basic equations of turbulence in gas–liquid two-phase flow. Int. J. Multiphase Flow 15 (5), 843–885.

Lamb, H., 1932. Hydrodynamics, sixth ed. Cambridge University Press, New York.

Launder, B.E., Spalding, D.B., 1974. The numerical computation of turbulent flows. Comput. Meth. Appl. Mech. Eng. 3, 269–289.

Liu, T.J., 1998. The role of bubble size on liquid phase turbulent structure in two-phase bubbly flow. In: Proceedings of Third International Congress on Multiphase Flow, CD ROM Publication, ICMF'98, June 8–12, Lyon, France.

Lopez de Bertodano, M.A., 1992. Turbulent bubbly two-phase flow in a triangular duct. Ph.D. dissertation, Rensselaer Polytechnic Institute.

Marié, J.L., Moursali, E., Tran-Cong, S., 1997. Similarity law and turbulence intensity profiles in a bubble layer at low-void fractions. Int. J. Multiphase Flow 23, 227–247.

Moraga, F.J., Bonetto, R.T., Lahey, R.T., 1999. Lateral forces on spheres in turbulent uniform shear flow. Int. J. Multiphase Flow 25, 1321–1372.

Morel, C., 1997. Turbulence modeling and first numerical simulations in turbulent two-phase flows. Report SMTH/LDMS/97-023, October, CEA/Grenoble, France.

Nakoryakov, V.E., Kashinsky, O.N., Burdukov, A.P., Odnoral, V.P., 1981. Local characteristics of upward gas–liquid flows. Int. J. Multiphase Flow 7, 63–81.

Nakoryakov, V.E., Kashinsky, O.N., Randin, V.V., Timkin, L.S., 1996. Gas–liquid bubbly flow in vertical pipes. ASME J. Fluids Eng. 118, 377–382.

Sato, Y., Sadatomi, M., Sekoguchi, K., 1981. Momentum and heat transfer in two-phase bubble flow. Parts I and II. Int. J. Multiphase Flow 7, 167–190.

Serizawa, A., Kataoka, I., Michiyoshi, I., 1975. Turbulence structure of air–water bubbly flow. Parts I–III. Int. J. Multiphase Flow 2, 221–259.

Troshko, A.A., 2000. Two-equation, multi-dimensional model of turbulence in bubbly flows. Ph.D. dissertation, Texas A&M University.

Troshko, A.A., Hassan, Y.A., 2001. Law of the wall for two-phase turbulent boundary layers. Int. J. Heat Mass Transfer 44 (4), 871–875.

Wang, S.K., Lee, S.J., Jones, O.C., Lahey, R.T., 1987. 3D turbulence structure and phase distribution measurements in bubbly two-phase flows. Int. J. Multiphase Flow 13 (3), 327–343.